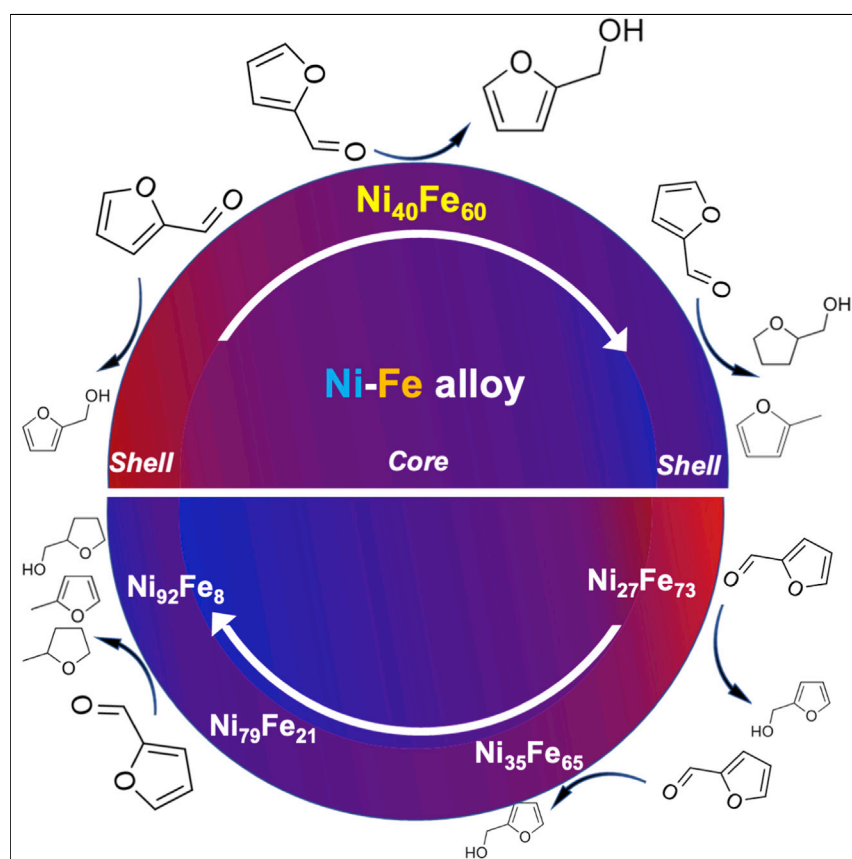


Article

Probing the core and surface composition of nanoalloy to rationalize its selectivity: Study of Ni-Fe/SiO₂ catalysts for liquid-phase hydrogenation

The synergy between two metals is a key parameter to selectively convert bio-sourced molecules to highly valued chemicals. However, to do that, the distribution of base metals in bimetallic structures must be controlled. We showed that alloying nickel and iron, two of the most common metals, permitted us to obtain stable and very active catalyst. A detailed characterization of the materials provides useful insight into the surface composition needed to understand the high catalytic reactivity and selectivity of Ni-Fe structures.

Dichao Shi, Achraf Sadier,
Jean-Sébastien Girardon, ...,
Sébastien Paul, Robert
Wojcieszak, Eric Marceau

robert.wojcieszak@univ-lille.fr (R.W.)
eric.marceau@univ-lille.fr (E.M.)

Highlights

Bimetallic Ni-Fe catalysts in
hydrogenation of furfural were
extensively studied

Fe as a promoter of Ni increases
catalyst selectivity and its stability

Ni concentration changed from
Ni-enriched core to Ni-depleted,
Fe-enriched outer shells

Limited-size Ni domains among
Fe atoms permit control of the
hydrogenation process



Shi et al., Chem Catalysis 2, 1686–1708
July 21, 2022 © 2022 Elsevier Inc.
<https://doi.org/10.1016/j.checat.2022.04.009>



Article

Probing the core and surface composition of nanoalloy to rationalize its selectivity: Study of Ni-Fe/SiO₂ catalysts for liquid-phase hydrogenation

Dichao Shi,¹ Achraf Sadier,¹ Jean-Sébastien Girardon,¹ Anne-Sophie Mamede,¹ Carmen Ciotonea,^{1,5} Maya Marinova,² Lorenzo Stievano,³ Moulay T. Sougrati,³ Camille La Fontaine,⁴ Sébastien Paul,¹ Robert Wojcieszak,^{1,*} and Eric Marceau^{1,6,*}

SUMMARY

Rationalization of the catalytic performance of bimetallic Ni-Fe catalysts in selective hydrogenation reactions is based on the Ni and Fe distribution within the nanoparticles and at their surface. By applying a combination of element-specific and surface-specific characterization techniques (⁵⁷Fe Mössbauer spectroscopy, X-ray absorption spectroscopy, and low-energy ion scattering) to a series of Ni-Fe/SiO₂ catalysts differing by their Ni and Fe molar proportions, we showed that reduced Ni-Fe nanoparticles exhibit a gradient of Ni concentrations from a Ni-enriched core to Ni-depleted, Fe-enriched outer shells. A surface proportion of 35–45 Ni atom % showed the highest yield of furfuryl alcohol in liquid-phase hydroconversion of furfural. These results point to the need for Ni surface domains of limited size among Fe atoms to restrict the hydroconversion process to its first stage rather than to nominal compositions of the catalyst or to surface sites that would appear to be particularly selective per se.

INTRODUCTION

Furfural (FF) is a furanic aldehyde produced industrially since the 1930s by dehydration of xylose, a pentose present in hemicellulose.^{1–4} Several molecules of interest can be derived from FF through successive or parallel reactions with hydrogen. Furfuryl alcohol (FFA), obtained by hydrogenation of the aldehyde function of FF, is an intermediate in production of fine chemicals, fibers, and rubbers.

Secondary and tertiary products of hydroconversion, such as 2-methylfuran (MF), tetrahydrofurfuryl alcohol (THFFA), and 2-methyltetrahydrofuran (MTHF) are used as solvents, fuel additives, or chemical intermediates and are obtained by hydrogenolysis and/or hydrogenation of the furan ring of FFA.^{5–7} The selectivity of the catalyst employed in hydroconversion of FF is thus of paramount importance when one of these products is targeted in particular. Restricting the transformation of FF to FFA requires a catalyst on which over-hydrogenation and hydrogenolysis reactions are avoided.

Noble metals have largely been employed for liquid-phase hydroconversion of bio-sourced molecules, but they are costly, and their abundance is low.^{8–13} Ideally, substitutes should be found among the more abundant and cheaper first-row transition metals. Although cobalt- and copper-based systems have been tested for being

The bigger picture

Bimetallic catalysis for conversion of bio-sourced molecules has often relied on noble metals that should be replaced in the near future by the association of cheaper and more abundant base metals, also known by a poor Z-contrast, which makes in-depth characterization of these systems challenging. However, determining the distribution of base metals in bimetallic nanoparticles is of paramount importance if one wants to rationalize their selectivity. Besides demonstrating that, despite their oxidable character, Ni-Fe catalysts are stable systems for liquid-phase hydroconversion of furfural, this study demonstrates that heterogeneities in the structure of reduced Ni-Fe nanoparticles are key to understanding their catalytic properties, provides a characterization methodology to discriminate between their surface and core compositions, and determines an adequate balance between the two metals that allows tuning the relative rates of the various reaction pathways and, thus, the selectivity.

selective to FFA, but with issues of stability and deactivation,^{2,4} nickel, in contrast, is known for its high activity and poor selectivity because it catalyzes hydrogenation of oxygenated functions and aromatic rings, hydrodeoxygenation reactions, and decarbonylation reactions.^{14–22} However, tuning the catalytic performance of Ni can be done by association with a second metal within bimetallic nanoparticles. In recent years, Fe has been shown to be a promising and cost-effective candidate for preparation of selective Ni-based systems. A Ni₇₅Fe₂₅/Al₂O₃ catalyst prepared by Putro et al.²¹ (where the two figures correspond to the molar proportions of the metals in the catalyst) provided a 92% yield of FFA in isopropanol at 150°C, whereas the fully hydrogenated molecule, THFFA, was the main product formed with Ni/Al₂O₃ (selectivity, 61%).¹⁴ This tendency was confirmed by Shi et al.²³ under similar conditions using a Ni₆₂Fe₃₈/SiO₂ catalyst. A high yield of FFA was also obtained in ethanol by Chieffi et al.²⁴ using Ni₅₈Fe₄₂/C (conversion of FF, 99%; selectivity to FFA, 90%) and, more generally, in protic solvents by Jia et al.²⁵ using a Ni₇₅Fe₂₅/SiO₂ catalyst (conversion of FF in methanol, >99%; selectivity to FFA, 97%) (Table S1). Addition of water to methanol would lead to cyclopentanone by ring rearrangement.²⁶ These results in the liquid phase parallel the reported selectivity to FFA of Ni-Fe catalysts used in vapor-phase conversion of FF^{27,28} and their selectivity to 2,5-furandimethanol in hydrogenation of 5-hydroxymethylfurfural in butanol.²⁴ The current literature has mostly focused on a narrow range of Ni-Fe nominal formulations, roughly between Ni₆₀Fe₄₀ and Ni₈₀Fe₂₀, leaving open the question of the behavior of Fe-richer or Ni-richer systems.

Understanding the catalytic performance of Ni-Fe nanoparticles as a function of their formulation requires one to understand what lies at their surface. The Ni and Fe distribution at the surface of Ni-Fe nanoparticles has been assumed to influence their hydroconversion properties.²⁹ Oxophilic Fe has been suggested to favor adsorption of oxygenated functions, whereas density functional theory (DFT) calculations and experimental measurements tend to indicate that alloyed or Fe-rich domains hinder adsorption of aromatic rings compared with Ni.^{14,16,20,30–33}

Three aspects must be taken into account when one wants to draw firm correlations between the catalytic properties of Ni-Fe catalysts and the composition of nanoparticles and determine whether the nominal composition of the catalyst is the relevant parameter to rationalize catalytic performance. First, to avoid issues linked to structure sensitivity and the existence of a diversity of active sites, Ni-Fe nanoparticles must have a similar size and composition throughout the catalyst, which is difficult to attain with standard preparation methods, such as incipient wetness impregnation,^{34–36} but can be achieved using deposition-precipitation.^{23,37} Second, it must be checked whether the two metals are alloyed in a homogeneous manner in the particles, core, and outer shells or whether they are segregated. Reports of heterogeneous distributions of the metals in a given Ni-Fe nanoparticle can be found in the literature.^{20,38} Last, with Ni and Fe being base metals prone to oxidation, questions are raised regarding the reversibility of metal dealloying or re-alloying when switching between an oxidizing environment, such as exposure to air, and a reducing environment, such as the initial reduction or re-activation in H₂. For example, dealloying has been shown by X-ray absorption spectroscopy for Ni-Fe nanoparticles used for dry reforming of methane.³⁹ Answering these questions requires not only characterization methods at the nanometer scale but also their implementation under *in situ* conditions.

The objective of this work is to link the activity and selectivity of Ni-Fe catalysts in liquid-phase hydrogenation of FF to the distribution of the two elements in and at

¹Université Lille, CNRS, Centrale Lille, Université Artois, UMR 8181 – UCCS – Unité de Catalyse et Chimie du Solide, 59000 Lille, France

²Université Lille, CNRS, INRAE, Centrale Lille, Université Artois, FR 2638-IMEC-f Michel-Eugène Chevreul, 59000 Lille, France

³Institut Charles Gerhardt de Montpellier, UMR 5253, Université de Montpellier/CNRS/ENSCM, Pôle Chimie Balard Recherche CC 043, 1919 route de Mende, Cedex 5, 34293 Montpellier, France

⁴Synchrotron SOLEIL, Beamline ROCK, L'Orme des Merisiers, 91190 Saint-Aubin, France

⁵Unité de Chimie Environnementale et Interactions sur le Vivant (UCEIV, EA 4492), SFR Condorcet FR CNRS 3417, Université du Littoral Côte d'Opale (ULCO), 145 Av. M. Schumann, 59140 Dunkerque, France

⁶Lead contact

*Correspondence:
robert.wojcieszak@univ-lille.fr (R.W.),
eric.marceau@univ-lille.fr (E.M.)

<https://doi.org/10.1016/j.checat.2022.04.009>

the surface of the bimetallic nanoparticles. This distribution will be evaluated for a series of Ni-Fe/SiO₂ catalysts exhibiting different molar proportions of the two metals along the various stages between the initial reduction of the catalyst in hydrogen and the catalytic test. A set of complementary characterization techniques will selectively inform on each element (X-ray absorption spectroscopy and ⁵⁷Fe Mössbauer spectroscopy), provide access to atomic-resolution analysis (high-resolution transmission electron microscopy coupled with high-resolution electron energy loss spectroscopy), and probe the outer shells of the nanoparticles (low-energy ion scattering spectroscopy). In this way, it will be determined to what extent the bulk composition of the nanoparticles is reflected in their surface composition, whether reversible or irreversible changes occur during the catalyst's life, and how the surface characteristics of the Ni-Fe nanoparticles condition their selectivity toward FFA or other reaction products.

RESULTS

Characterization of Ni-Fe nanoparticles after reduction at 700°C and exposure to air

All XRD (X-ray diffraction) patterns recorded under ambient conditions after reduction at 700°C evidence three diffraction peaks at about 43–44°, 50–51°, and 74–75°, assigned to the (111), (200), and (220) reflections of fcc metallic phases and close to the positions expected for fcc Ni (Figure S1). No metal segregation between particles of different structures (for example, bcc Fe-based particles) was evidenced. The diffraction peaks were shifted toward larger angles (i.e., interplanar distances were smaller) when the Ni molar proportion increased, and the value of the unit cell parameter *a*, calculated from the (200) reflection to avoid any possible interference with the NiO (200) peak at 43.4°, decreased (Table S2). This is in line with the slightly smaller atomic radius of Ni compared with that of Fe (0.124 versus 0.126 nm) and indicates that the two metals are alloyed at least in the crystalline core of the nanoparticles. In a previous work,²³ and in line with the literature,⁴⁰ the unit cell parameter *a* of Ni-Fe alloys was shown to decrease linearly with the increasing Ni content. This Vegard's law was used for a rough assessment of the atomic proportions of Ni and Fe in the crystalline core of the particles. Analysis by XRD, XRF (X-ray fluorescence), and ICP-OES (inductively coupled plasma optical emission spectrometry) led to consistent results (Table 1). The values deduced from Vegard's law inform on the average composition of the nanoparticles but not on the possible existence of heterogeneities. The specific surface area of the reduced catalysts, calculated with the BET (Brunauer, Emmett, and Teller) model, is also presented in Table 1, and its evolution with the Ni proportion will be discussed below. Bright-field TEM (transmission electron microscopy) was used to determine the particle size distribution (Figure S2). Narrow size distributions centered in the 4- to 7-nm range were found for all catalysts. The values of the average particle size are consistent with those calculated from the XRD patterns using the Scherrer equation (5–6 nm) (Table S3). Because the adsorptive properties of the particles depend on their surface composition, and the adsorption stoichiometries of the usual probe molecules are not known for Ni-Fe surfaces, the fraction of surface atoms, or dispersion *D* (%), was evaluated from the size histograms rather than from chemisorption measurements. The formula $97.1/\varnothing$ (nm), formerly used for hemispherical nanoparticles of fcc Ni, was applied to each class of diameter \varnothing from the histograms. Values of *D* ranged from 17%–19% (Table S3). The metal surface area exposed per gram of catalyst was between 62 and 73 m² gcat^{−1}, assuming that one Ni or Fe atom occupies 6.3 Å² (Table S3).^{41,42}

A few individual Ni-Fe nanoparticles on catalysts Ni₅₅Fe₄₅/SiO₂, Ni₆₂Fe₃₈/SiO₂, Ni₇₃Fe₂₇/SiO₂, and Ni₈₄Fe₁₆/SiO₂ were studied by STEM-EELS (scanning TEM with

Table 1. Proportions of Ni and Fe in the DPU solutions and characteristics of the reduced catalysts: metal loading, molar proportions of Ni and Fe, and specific surface area

Samples	Proportions of Ni and Fe in DPU solutions		Metal loading and molar proportions of Ni and Fe after reduction at 700°C					Specific surface area (m ² g ⁻¹)
	Ni (%)	Fe (%)	Metal loading (Ni + Fe wt %) ^a	Ni (%) ^a	Fe (%) ^a	Ni (%) ^b	Fe (%) ^b	
Ni ₃₅ Fe ₆₅ /SiO ₂	25	75	63	35	65	35	65	136
Ni ₅₅ Fe ₄₅ /SiO ₂	40	60	49	55	45	55	45	162
Ni ₆₂ Fe ₃₈ /SiO ₂	50	50	49	62	38	63	37	238
Ni ₇₃ Fe ₂₇ /SiO ₂	60	40	54	73	27	71	29	224
Ni ₈₄ Fe ₁₆ /SiO ₂	75	25	55	84	16	84	16	178
Ni ₉₂ Fe ₈ /SiO ₂	90	10	58	92	8	89	11	135
Ni ₁₀₀ /SiO ₂	100	0	59	100	0	100	0	137

DPU, deposition precipitation with urea.

^aObtained from XRF/ICP studies.^bObtained from XRD studies.

electron energy loss spectroscopy) coupled to HAADF (high-angle annular dark-field imaging) to evidence heterogeneities in the nanoparticles (Figure 1). The choice of catalysts was based on relevance with respect to their very different catalytic properties despite similar metal specific surface areas and the sensitivity of the technique. In all cases, Ni-Fe nanoparticles from catalysts exposed to air exhibited a core-shell structure. The composition of the Ni-Fe alloyed core matched the composition deduced from XRD, but a 0.5- to 1-nm-thick oxidized shell (EELS measurements are given in Figure S3 as an example) appeared to be depleted of Ni by 10%–40%. On some images (HAADF and EELS elemental maps; see, for instance, Figures 1B1 and 2), it can be seen that the Fe-rich shell developed in an asymmetrical way and not all around the particles. The measured compositions of the cores of the scanned particles are given in Table S4. The standard deviation for Fe was 7 atom %, but it must be acknowledged that the number of nanoparticles that could be investigated during the microscopy run was limited and, thus, not statistically significant. This value is consistent with the standard deviation of 8 atom % presented in our previous work for a Ni₆₂Fe₃₈/SiO₂ catalyst and calculated from EDX (energy-dispersive X-ray analysis) measurements with larger sampling of particles.²³ Despite the very different metal fractions, DPU (deposition-precipitation with urea) synthesis leads to Ni-Fe particles with similar crystal structures (alloyed fcc particles), similar narrow size distributions (low fraction of particles smaller than 3 nm or larger than 8 nm), similar metal dispersion, and, with respect to individual compositions, similar standard deviations (no monometallic particles, few particles with very large discrepancies in composition). After exposure to air, the bimetallic nanoparticles possess a Ni-Fe alloyed core and a Fe-enriched oxidized shell, in line with a previous observation by STEM-EDX.²⁰

Characterization of Ni-Fe nanoparticles after reduction at 700°C: *in situ* measurements under H₂

In situ Mössbauer spectroscopy was used to determine whether the segregation of Fe toward the surface was already present prior to exposure to air or whether it was a consequence of it. Dried samples were reduced in H₂ at 700°C and transferred to a gas-flow cryostat under a protected atmosphere. Mössbauer spectra measured at 5 K on the four as-reduced samples investigated by STEM-HAADF are shown in Figure 2. All samples exhibited a dominant contribution from Fe(0) in a magnetic environment, in all cases exceeding 90% of the total resonance area. Spectra were fitted with two sextets and slightly different hyperfine fields (blue curves). Decomposition

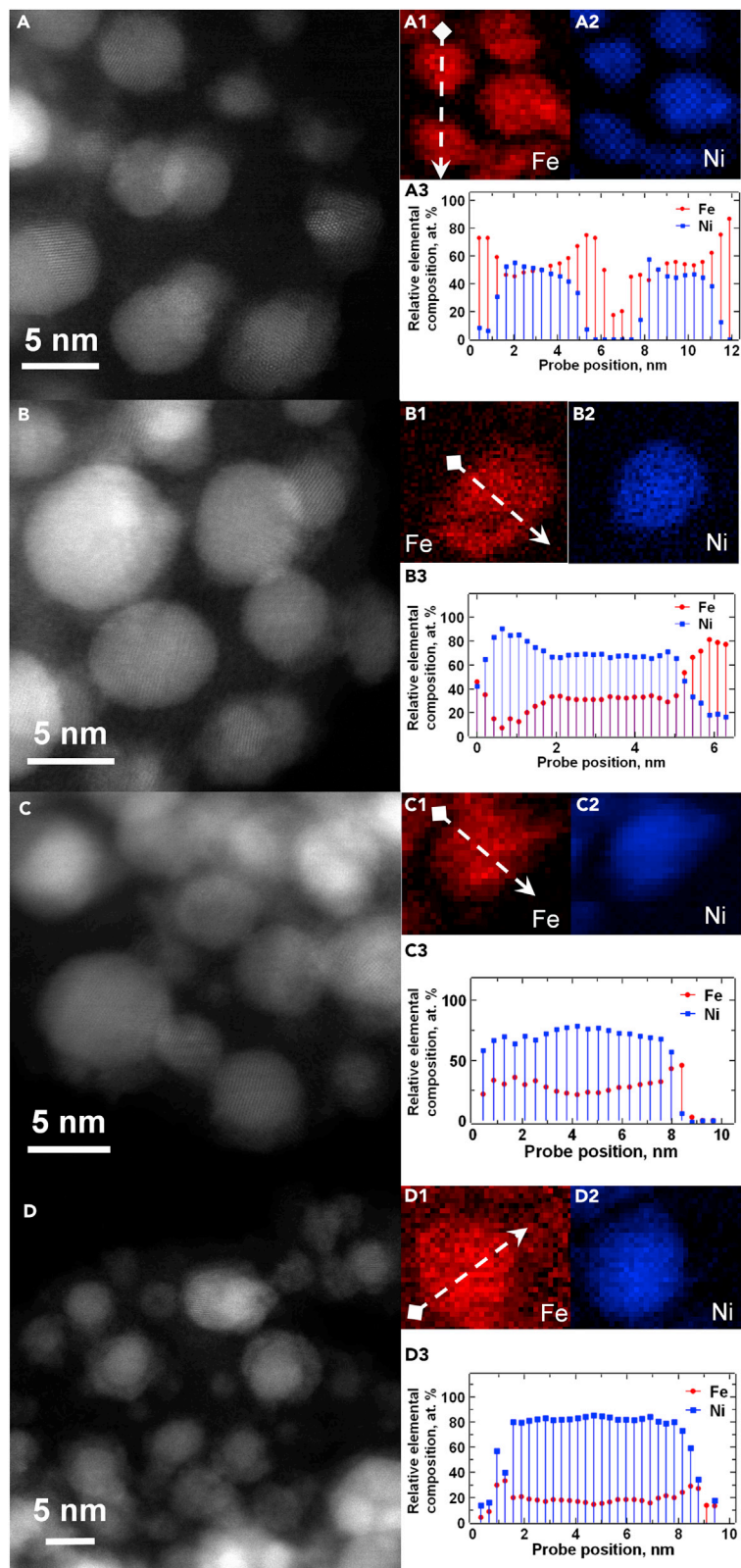


Figure 1. STEM-HAADF images and elemental maps for the Fe-L_{3,2} edge at 710.5 eV and Ni-L_{3,2} edge at 856.5 eV

- (A) Ni₅₅Fe₄₅/SiO₂.
(B) Ni₆₂Fe₃₈/SiO₂.
(C) Ni₇₃Fe₂₇/SiO₂.
(D) Ni₈₄Fe₁₆/SiO₂.

All were obtained by STEM-EELS mapping after reduction at 700°C and exposure to air.

into two Fe(0) components was also reported in the literature for Mössbauer spectra recorded at room temperature on Ni-Fe nanoparticles supported on carbon.³⁸ This procedure does not necessarily imply the existence of two separate domains but corresponds to a simplified way of dealing with the existence of gradients of concentrations in a continuum of environments in the material (supplemental experimental procedures, p. S30). The isomer shifts were in the range typically observed for Fe(0) in Ni-Fe alloys,⁴³ and the corresponding values of the hyperfine field B_{HF} , close to 29–30 and 33 T (Table 2), are characteristic of Ni-Fe alloys in which Ni or Fe is the major metal, respectively.⁴⁴ In addition to these two components, a minor component accounting for about 10% of the total resonance area was present at the center of the spectrum and can be attributed to traces of divalent or trivalent iron, which were not totally reduced in the reactor (green curves), or to traces of reduced Fe(0) in non-magnetic environments (red curve).

Given the homogeneity in particle size and individual composition observed by TEM after exposure to air, the existence of different contributions for Fe(0) is consistent with an uneven distribution of Fe within the Ni-Fe particles, between a Ni-rich core (lower value of B_{HF}) and Fe-rich domains presumably in the outer shells (higher value of B_{HF}). The lower value of B_{HF} decreases from 30.4 to 28.8 T (the value of B_{HF} expected for pure Ni) when the Ni proportion in the core of the particles increases, in agreement with XRD and TEM measurements. The enrichment in Fe when moving toward the surface thus predates the exposure to air and can be related to the late reduction of this metal compared with Ni.²³

Evolution of the reduced Ni-Fe nanoparticles upon exposure to an oxidizing atmosphere

To get insight into the process of oxidation of reduced Ni-Fe nanoparticles, oxidation of reduced samples Ni₆₂Fe₃₈/SiO₂ and Ni₈₄Fe₁₆/SiO₂ was followed by quick X-ray absorption spectroscopy at 80°C, a temperature chosen to allow better thermal control (Figures S4A and S4B). Recording of the spectra started while the catalysts reduced *in situ* were still kept in an H₂ atmosphere, making it possible to identify the very moment when oxidation would start. After a purge in N₂, the catalysts were exposed to diluted O₂. Summation over 10 spectra was performed to reduce the noise, and the gap between two points in Figure S4A corresponds to a time difference of 5 s. The kinetics of oxidation were extracted using an MCR-ALS (multivariate curve resolution alternating least square) analysis procedure restricted to the X-ray absorption near edge structure (XANES) region. Two components arose from the chemometrics analysis, one corresponding exactly to the initial, reduced metals, the other one to the oxidized elements (Ni²⁺ and Fe³⁺, respectively, by comparison with the XANES spectra of NiO and Fe₂O₃; Figure S4B). For the two catalysts, oxidation took place in two stages. The very rapid first stage converted 20% of Ni and 30%–40% of Fe to the oxidic form within the first 25 s. Oxidation would then proceed more progressively without reaching an asymptotic value during the 30 min the measurements lasted. It can thus be anticipated that storage in ambient air would also end with slow and progressive oxidation of the nanoparticles, with the proportion of oxidic phases in a given sample depending on the duration of the storage period.

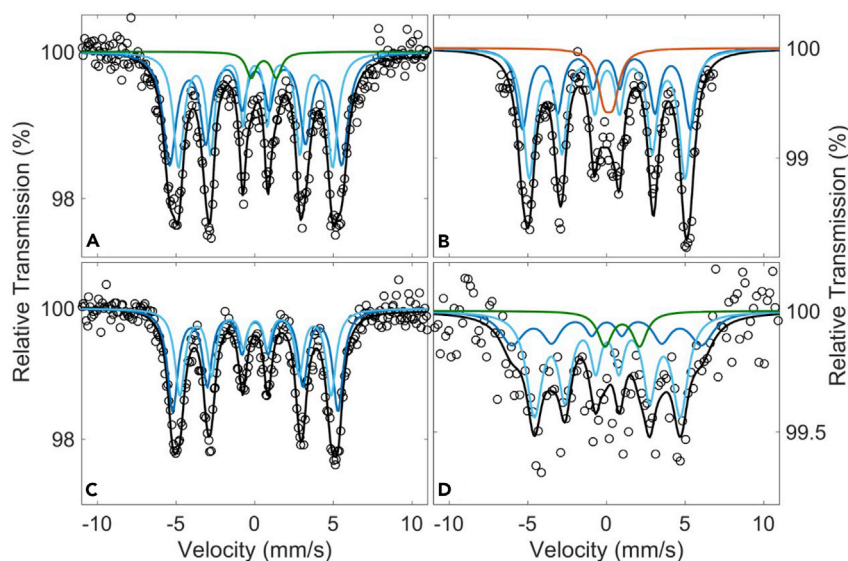


Figure 2. ^{57}Fe Mössbauer spectra measured at 5 K after reduction in H_2 flow at 700°C

(A) $\text{Ni}_{15}\text{Fe}_{45}/\text{SiO}_2$.

(B) $\text{Ni}_{62}\text{Fe}_{38}/\text{SiO}_2$.

(C) $\text{Ni}_{73}\text{Fe}_{27}/\text{SiO}_2$.

(D) $\text{Ni}_{84}\text{Fe}_{16}/\text{SiO}_2$.

Characterization of Ni-Fe nanoparticles upon and after re-activation under H_2

Before the catalytic test, Ni-Fe/ SiO_2 catalysts stored in air must be re-activated under H_2 to restore their metallic character. The process of reduction of the oxidized fractions was first explored by temperature-programmed reduction experiments followed by quick X-ray absorption spectroscopy (XAS) (Figures 3 and S5). Spectra were recorded at the Ni and Fe K edges under *in situ* conditions during a ramp in H_2 up to 500°C . A quantitative analysis was carried out using the MCR-ALS procedure. To better extract the oxidized components from the mixture of oxidic and reduced species, each catalyst was calcined in air in a muffle oven at 200°C for 10 h, and the spectrum from fully oxidized Ni or Fe, recorded *ex situ*, was added to the MCR-ALS matrix. The initial proportion of metallic Fe was also determined by a preliminary MCR-ALS analysis carried out on a matrix of initial spectra. The inclusion of the EXAFS (extended X-ray-absorption fine structure) region in the MCR-ALS procedure did not lead to identification of oxides with precisely known structures, suggesting the existence of poorly defined Ni^{2+} - Fe^{3+} mixed phases in the oxidic fraction, and the MCR-ALS analysis was applied only to the XANES region.

The MCR-ALS analysis at the Ni K edge yielded only two contributions, Ni^{2+} and metallic Ni. The MCR-ALS analysis at the Fe K edge yielded three contributions, assigned according to the position of the edge with respect to reference compounds: Fe^{3+} ions, transforming into intermediate Fe^{2+} , and finally metallic Fe. Initially, the fraction of oxidized Fe was found to be larger than the fraction of oxidized Ni, in line with the observations presented earlier. An example of evolution during the temperature ramp is given in Figure 3 for catalyst $\text{Ni}_{35}\text{Fe}_{65}/\text{SiO}_2$ (the corresponding figures for four other catalysts are presented in Figure S5; measurements were not performed on $\text{Ni}_{92}\text{Fe}_8/\text{SiO}_2$ for sensitivity issues at the Fe K edge). Fe^{3+} ions started to transform into Fe^{2+} ions at 120°C . The reduction of the oxidized Ni fraction to metallic Ni took place in the 240°C – 350°C range. The reduction of Fe^{2+} to metallic Fe started at 295°C . It was confirmed in the study of the other catalysts that the final

Table 2. ^{57}Fe Mössbauer hyperfine parameters at 5 K of samples $\text{Ni}_{55}\text{Fe}_{45}/\text{SiO}_2$, $\text{Ni}_{62}\text{Fe}_{38}/\text{SiO}_2$, $\text{Ni}_{73}\text{Fe}_{27}/\text{SiO}_2$, and $\text{Ni}_{84}\text{Fe}_{16}/\text{SiO}_2$ after reduction at 700 °C

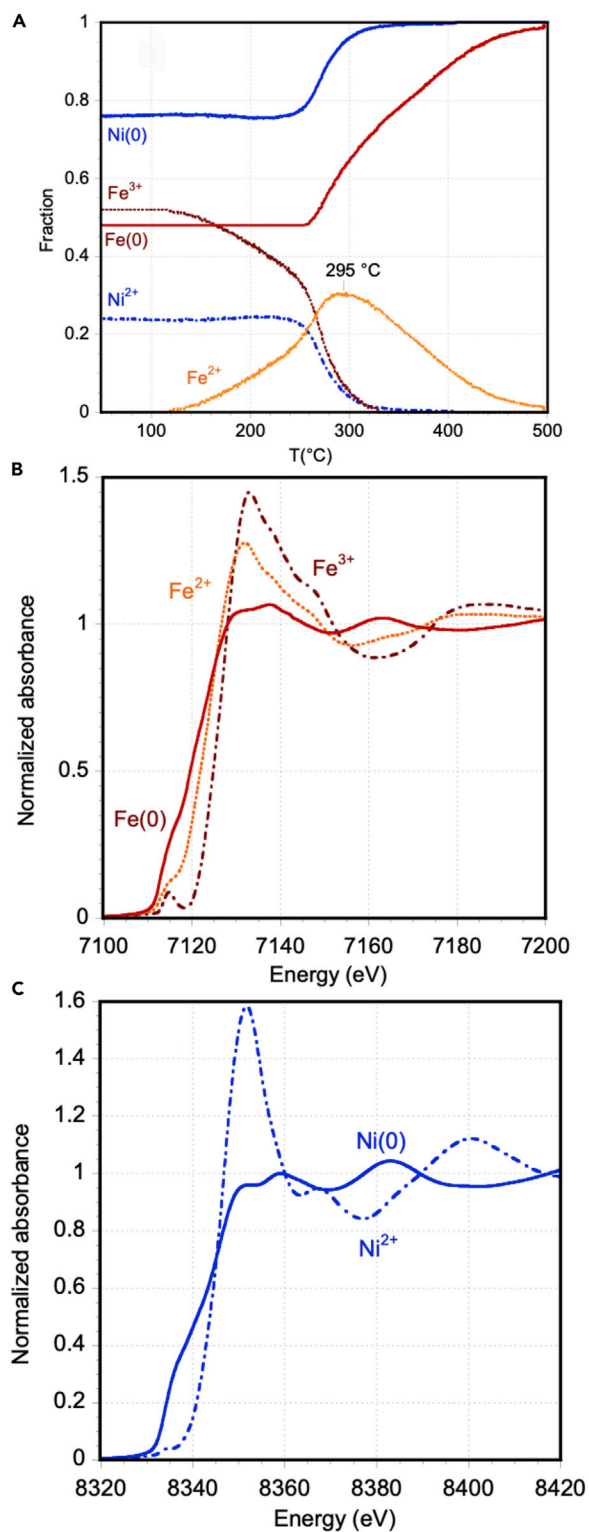
Sample	Site	δ (mm s $^{-1}$)	Δ (mm s $^{-1}$)	Γ (mm s $^{-1}$)	Area (%)	B_{HF} (T)
$\text{Ni}_{55}\text{Fe}_{45}/\text{SiO}_2$	Fe(0), Ni-Fe core Fe(0), Ni-Fe surface Fe(II)	0.15 ± 0.01 0.17 ± 0.02 1.16 ± 0.08	$0.0 \pm 1.6 \pm 0.1$	0.8 ± 0.1 1.0 ± 0.1 0.8 ± 0.1	44 ± 5 52 ± 5 4 ± 2	30.4 ± 0.2 33.9 ± 0.3 -
$\text{Ni}_{62}\text{Fe}_{38}/\text{SiO}_2$	Fe(0), Ni-Fe core, Fe(0), Ni-Fe surface, Fe(0), non-magnetic	0.15 ± 0.02 , 0.10 ± 0.02 , 0.24 ± 0.04	$0, 0, 0.6 \pm 0.1$	0.9 ± 0.1 , 0.9 ± 0.1 , 1.0 ± 0.1	55 ± 8 , 35 ± 8 , 10 ± 1	29.8 ± 0.3 , 33.1 ± 0.4 , -
$\text{Ni}_{73}\text{Fe}_{27}/\text{SiO}_2$	Fe(0), Ni-Fe core, Fe(0), Ni-Fe surface	0.1 ± 0.2 , 0.2 ± 0.2	0, 0	1.1 ± 0.1 , 0.8 ± 0.1	63 ± 9 , 37 ± 9	29.4 ± 0.2 , 33.6 ± 0.9
$\text{Ni}_{84}\text{Fe}_{16}/\text{SiO}_2$	Fe(0), Ni-Fe core, Fe(0), Ni-Fe surface, Fe(II)	0.16 ± 0.04 , 0.1 ± 0.2 , 1.2 ± 0.1	$0, 0, 2.2 \pm 0.1$	1.2 ± 0.1 , 1.8 ± 0.2 , 1.1 ± 0.1	61 ± 7 , 29 ± 7 , 10 ± 3	29.8 ± 0.5 , 36 ± 2 , -

δ , isomer shift; Δ , electric quadrupole splitting; Γ , line width at half maximum; B_{HF} , magnetic hyperfine field.

stage of reduction for Fe leveled off when the fraction of metallic Ni exceeded 80%–85%. The activation process of Ni and that of Fe were linked, and the reduction of Fe was governed by the proportion of Ni in the nanoparticles; the onset of the reduction of Fe^{3+} to Fe^{2+} ions shifts from 130 °C for $\text{Ni}_{35}\text{Fe}_{65}/\text{SiO}_2$ to 60 °C for $\text{Ni}_{84}\text{Fe}_{16}/\text{SiO}_2$. The larger the Ni molar proportion, the lower the temperature range for Ni reduction to the metallic state and the lower the temperature at which Fe reverted to its metallic state. The more Ni in the NPs (nanoparticles), including in the oxidized surface fraction, the easier the reduction of this oxidized fraction to form surface reduced Ni centers (the fractions of Ni^{2+} and Fe^{3+} belong to approximately the same range in Figures 3 and S6, but the Ni nominal proportion in the NPs increases along the series, meaning that the Ni content in the oxidized fraction increases). When these surface-reduced centers have appeared, H_2 can be readily activated and “spill over” to provoke the reduction of Fe ions to the metallic state.^{20,29,45,46}

The structural characteristics of the re-activated nanoparticles, obtained by fitting the EXAFS oscillations and Fourier transforms at the Ni and Fe K edges for the first shell of neighboring atoms, correspond to the features described above (see detailed analysis in Figures S6 and S7 and Tables S5–S8). In brief, the four peaks observed on the Fourier transforms for the two metals, similar to those obtained for a Ni foil in terms of relative intensity and position, indicate that nickel and iron appeared predominantly in the metallic state and in the fcc structure of the original bimetallic nanoparticles. At the Ni K edge, the number of nearest neighbors was found to be higher than 10.7, which is consistent with the presence of Ni mostly in the core of the particles. The number of metallic neighbors around Fe was between 8 and 9, and an oxygen contribution at a low distance had to be added. This discrepancy with respect to Ni has been reported several times in the literature and attributed to the existence of Fe-enriched shells,^{30,34,47–49} a hypothesis strengthened by our own analysis of the nanoparticle composition. At the Ni and Fe K edges, Ni-Fe interatomic distances R were found to consistently decrease when increasing the Ni molar proportion, in line with the decrease of the cell parameter a determined by XRD. For each catalyst, the confidence intervals evaluated around R at the two edges overlapped and were in very good agreement.

Because temperature-programmed reduction (TPR) is governed by kinetics, and re-activation in H_2 prior to the catalytic test takes place at 400 °C only, the state of re-activated catalysts was also checked by applying Mössbauer spectroscopy to $\text{Ni}_{55}\text{Fe}_{45}/\text{SiO}_2$ and $\text{Ni}_{84}\text{Fe}_{16}/\text{SiO}_2$ after a series of three successive treatments: reduction in H_2 at 700 °C, exposure to air at room temperature, and re-activation under H_2 at 400 °C. After re-activation, still under an H_2 atmosphere, the temperature was decreased to 5 K, and Mössbauer spectra were recorded. The hyperfine

**Figure 3. XAS**

(A) Concentration profiles obtained from MCR-ALS analysis of activation under H_2 of $\text{Ni}_{35}\text{Fe}_{65}/\text{SiO}_2$.

(B) Corresponding spectral components at the Ni K edge.

(C) Corresponding spectral components at the Fe K edge.

parameters and proportions of each contribution are presented in Table S9. They were globally unchanged with respect to the analysis performed after reduction at 700°C. It was similarly verified by XAS that, after the oxidizing treatment at 80°C, the EXAFS Fourier transforms corresponding to metallic fcc Ni and Fe were recovered after a step of re-activation in H₂ at 400°C.

In situ X-ray absorption and Mössbauer spectroscopies show that, for catalysts exposed to air, the reduction of the Ni oxidized fraction to the metallic state drives the reduction of the oxidized Fe fraction (the higher the Ni content, the easier the reduction of Fe) and that the state of the nanoparticles after re-activation at 400°C in H₂ is similar to that characterized after the initial reduction at 700°C. Thus, exposure of the catalysts to an oxidizing atmosphere does not induce an irreversible redistribution or dealloying of the metals.

Surface composition of Ni-Fe nanoparticles after re-activation under H₂

The techniques used above suggest an enhanced Fe proportion in the outer shells but do not probe these shells directly. In contrast, low-energy ion scattering (LEIS) is based on scattering of noble gas ions over the catalyst surface, and, after calibration on pure nickel and iron oxides (supplemental information), enables a direct assessment of the distribution of Ni and Fe atoms at the extreme surface of the irradiated particles. As the surface is progressively etched by the ion beam, gradients of concentrations from the uppermost layers to the layers below can be observed.

LEIS measurements were applied to the six Ni-Fe/SiO₂ catalysts after reduction at 700°C, exposure to air, and re-activation in H₂ at 400°C. Transfer from the activation cell to the analysis chamber took place under an ultra-high vacuum. The first recorded signals, at a very low ion dose, were not very intense and corresponded to removal of contamination (carbon, hydrogen, etc.) by the ion beam; they were excluded from quantification. The intensity of the signal reached a maximum for a cumulative dose of $0.5 \times 10^{15} \text{ Ne}^+ \text{ ions cm}^{-2}$, which corresponded to the theoretical analysis of 50% of a flat surface and was considered to show the atomic surface composition of the cleaned Ni-Fe nanoparticles. The cumulative ion dose was further increased to $7.8 \times 10^{15} \text{ Ne}^+ \text{ ions cm}^{-2}$ to progressively reveal the evolution of the composition in the outer shells, below the outermost layer. Given the lack of standardization for measurements on nanoparticles distributed over a porous support and the initial presence of contamination layers, translation of the results to a probed depth expressed in nanometers will not be attempted. To exemplify the evolution of the composition along the Ni-Fe series, signals recorded for an identical dose of $4.1 \times 10^{15} \text{ Ne}^+ \text{ ions cm}^{-2}$ are shown in Figure 4. The Ni molar proportion in the outer shells of the reduced Ni-Fe nanoparticles increases when the global Ni proportion increases in the catalyst, as can be seen from the increasing contribution of Ni to the LEIS signal (blue curves). But it is obvious that the Fe contribution dominates the signal for the first four catalysts, although only Ni₃₅Fe₆₅/SiO₂ contains more Fe than Ni in its nominal composition.

The profiles of the Ni molar proportion in the outer shells are shown as a function of the cumulative ion dose in Figure S8, and Table 3 presents the values for cumulative ion doses of $0.5 \times 10^{15} \text{ Ne}^+ \text{ ions cm}^{-2}$ (outermost probed layer), $7.8 \times 10^{15} \text{ Ne}^+ \text{ ions cm}^{-2}$, and in the middle of the range. In all cases, and in line with a measurement reported in the literature for a single catalyst,⁵⁰ the surface of the reduced nanoparticles is very significantly enriched in Fe; the absolute depletion of Ni is, on average, 20 atom % with respect to the nominal composition. On the other hand, the Ni molar proportion increases when moving deeper into the subsurface, which provides

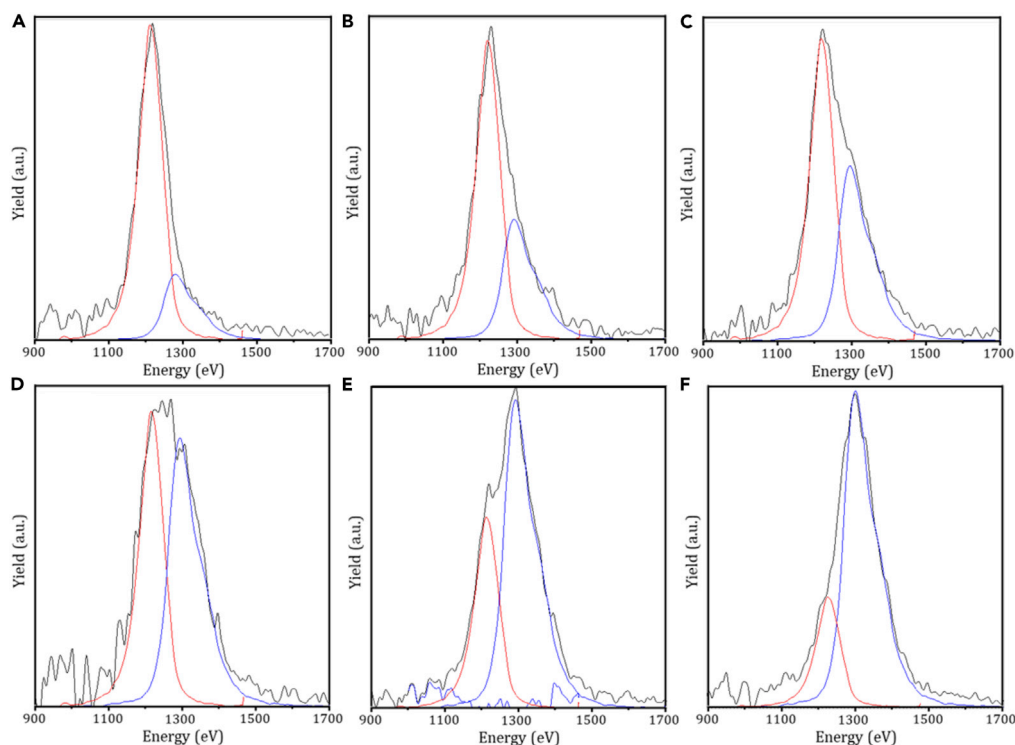


Figure 4. Decomposition of the LEIS spectra

(A) For $\text{Ni}_{35}\text{Fe}_{65}/\text{SiO}_2$.

(B) For $\text{Ni}_{55}\text{Fe}_{45}/\text{SiO}_2$.

(C) For $\text{Ni}_{62}\text{Fe}_{38}/\text{SiO}_2$.

(D) For $\text{Ni}_{73}\text{Fe}_{27}/\text{SiO}_2$.

(E) For $\text{Ni}_{84}\text{Fe}_{16}/\text{SiO}_2$.

(F) For $\text{Ni}_{92}\text{Fe}_8/\text{SiO}_2$.

All were measured at a cumulative iso-dose of $4.1 \times 10^{15} \text{ Ne}^+ \text{ ions cm}^{-2}$. Red, Fe contribution; blue: Ni contribution.

direct evidence of the existence of concentration gradients within the reduced nanoparticles, as suggested in the former sections. The increase in the Ni proportion is 10 atom %, on average, across the probed depth, but the gradient is steeper for catalysts with a higher proportion of Fe.

LEIS measurements directly confirm the existence of significant Fe enrichment and Ni depletion in the outer shells of the Ni-Fe reduced nanoparticles and of a concentration gradient when probing deeper inside the particles. The Ni atomic proportion in the outer shells still differs significantly from one catalyst to another, making comparison in catalysis relevant. Next, we will consider that the values reported in the

Table 3. Atomic proportions of Ni and Fe deduced from LEIS measurements as a function of the cumulative dose of $\text{Ne}^+ \text{ ions cm}^{-2}$

Catalyst	$0.5 \times 10^{15} \text{ Ne}^+$	$4.1 \times 10^{15} \text{ Ne}^+$	$7.8 \times 10^{15} \text{ Ne}^+$
$\text{Ni}_{35}\text{Fe}_{65}/\text{SiO}_2$	$\text{Ni}_{13}\text{Fe}_{87}$	$\text{Ni}_{19}\text{Fe}_{81}$	$\text{Ni}_{23}\text{Fe}_{77}$
$\text{Ni}_{55}\text{Fe}_{45}/\text{SiO}_2$	$\text{Ni}_{21}\text{Fe}_{79}$	$\text{Ni}_{32}\text{Fe}_{68}$	$\text{Ni}_{39}\text{Fe}_{61}$
$\text{Ni}_{62}\text{Fe}_{38}/\text{SiO}_2$	$\text{Ni}_{37}\text{Fe}_{63}$	$\text{Ni}_{39}\text{Fe}_{61}$	$\text{Ni}_{45}\text{Fe}_{55}$
$\text{Ni}_{73}\text{Fe}_{27}/\text{SiO}_2$	$\text{Ni}_{46}\text{Fe}_{54}$	$\text{Ni}_{50}\text{Fe}_{50}$	$\text{Ni}_{55}\text{Fe}_{45}$
$\text{Ni}_{84}\text{Fe}_{16}/\text{SiO}_2$	$\text{Ni}_{64}\text{Fe}_{36}$	$\text{Ni}_{66}\text{Fe}_{34}$	$\text{Ni}_{69}\text{Fe}_{31}$
$\text{Ni}_{92}\text{Fe}_8/\text{SiO}_2$	$\text{Ni}_{75}\text{Fe}_{25}$	$\text{Ni}_{77}\text{Fe}_{23}$	$\text{Ni}_{76}\text{Fe}_{24}$

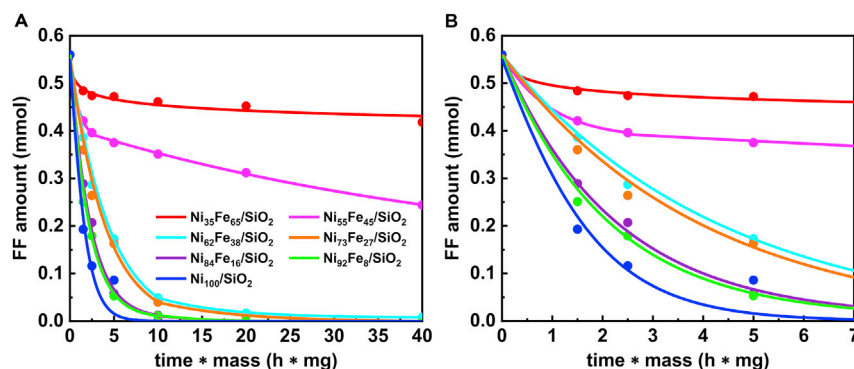


Figure 5. FF consumption for Ni-Fe/SiO₂ catalysts as a function of the (time × mass) product

(A) Whole curves.

(B) Right: zoom on the shorter time range.

Reaction conditions: T = 150°C; P(H₂) = 20 bar; solvent, isopropanol; volume of solution, 1.5 mL; m_{catalyst} = 3–10 mg; t = 0.5–4 h.

first column of Table 3 correspond to the composition of the outermost layer. Given that the analysis does not take place on a flat sample and that it cannot be guaranteed that the etching of the surface of nanoparticles supported on a porous oxide is done exactly layer by layer, we will conservatively add an absolute error bar extending to the value reported for a cumulative dose of 4.1×10^{15} Ne⁺.

Catalytic performance of Ni-Fe/SiO₂ and Ni/SiO₂ catalysts

After analyzing the core and surface distributions of Ni and Fe in the nanoparticles and ascertaining the reversibility of the changes taking places upon switching between oxidative and reducing atmospheres, the activity of the Ni-Fe catalysts in hydrogenation of FF was determined, compared with the monometallic Ni₁₀₀/SiO₂ catalyst, and correlated with their composition. In line with the preliminary catalytic measurements presented previously,²³ six reaction products were identified: the primary product, FFA, THFFA, MF, MTHF, and two ethers identified by gas chromatography-mass spectrometry (GC-MS), 2-(isopropoxymethyl)furan (iPrOMF), resulting from etherification of FFA with the isopropanol solvent, and 2-(isopropoxymethyl) tetrahydrofuran (iPrOMTHF), resulting from etherification of THFFA with isopropanol. THFFA, MF, and iPrOMF are secondary products resulting from transformation of FFA by hydrogenation of the furan ring, hydrogenolysis and etherification reactions, respectively. MTHF and iPrOMTHF are tertiary products. The reaction scheme is shown in Figure S9.

FF consumption was first compared as a function of the (time × mass) product. As shown in Figures 5 and S10, FF was not fully consumed using the two catalysts exhibiting the lowest Ni proportions, Ni₃₅Fe₆₅/SiO₂ and Ni₅₅Fe₄₅/SiO₂, even after 4 h with 10 mg of catalyst. Full conversion was achieved when the Ni content increased further. The richer the Ni content of the catalyst, the higher the activity for transformation of FF to FFA. The carbon balance was evaluated as a function of the (time × mass) product (Table S10). Only for Ni₃₅Fe₆₅/SiO₂ and Ni₅₅Fe₄₅/SiO₂ were carbon balances slightly lower than 90%. It can be hypothesized that, because of the low conversion, the FF concentration remained high in the reaction medium and resulted in its adsorption onto the surface of the catalysts. Products of degradation not detected by GC can also be responsible for the lower carbon balance. Conversely, carbon balances higher than 95% were achieved for Ni-rich catalysts. The product yield was plotted for each catalyst as a function of (time × mass)

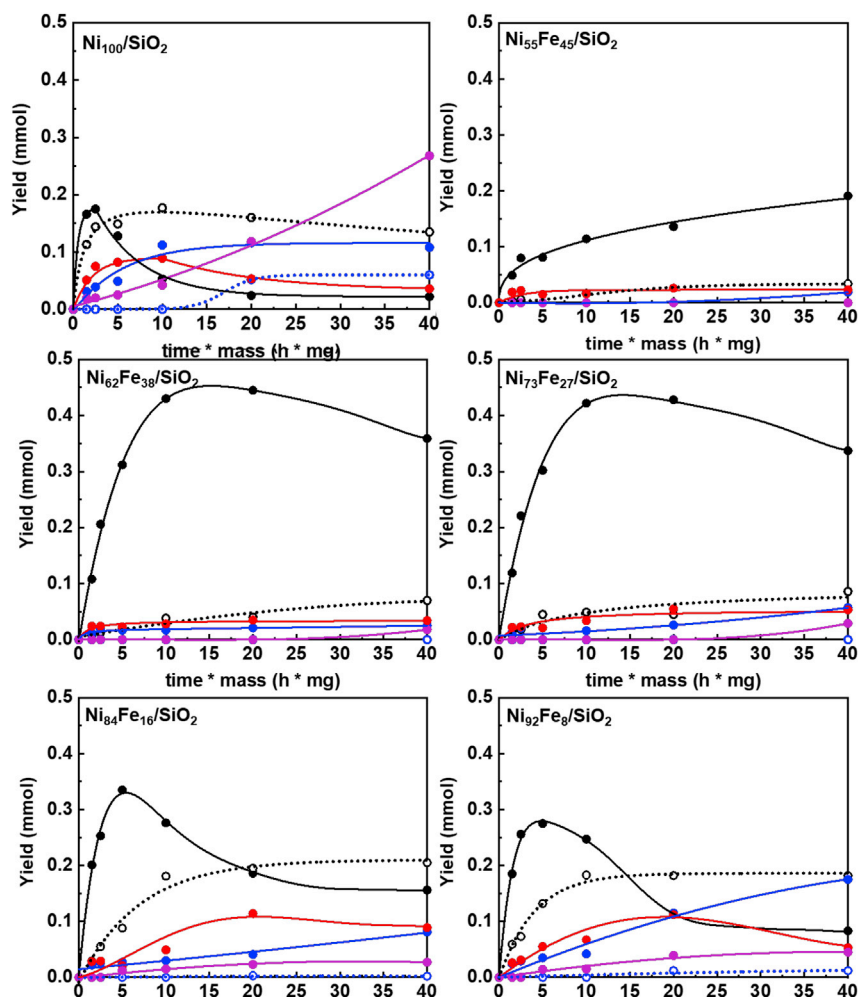


Figure 6. Yield of products as a function of (time \times mass)

Black lines (—●—), FFA; black dotted lines (---○---), iPrOMF; blue lines (—●—), THFFA; blue dotted lines (---○---), iPrOMTHF; red lines (—●—), MF; purple lines (—●—), MTHF. Reaction conditions: $T = 150^{\circ}\text{C}$; $P(\text{H}_2) = 20$ bar; solvent, isopropanol; volume of solution, 1.5 mL; $m_{\text{catalyst}} = 3\text{--}10$ mg; $t = 0.5\text{--}4$ h.

(Figure 6). For $\text{Ni}_{35}\text{Fe}_{65}/\text{SiO}_2$, the main product was FFA, even though it was produced in a very low amount that did not change with time (0.02 mmol). This may support the existence of a deactivation process caused by adsorption of FF or other derivatives on the active sites. Only after 4 h of reaction with 10 mg of catalyst would the hydrogenolysis product, MF, appear, but only as traces. $\text{Ni}_{55}\text{Fe}_{45}/\text{SiO}_2$ was also selective to FFA, giving a higher yield. Other products, such as the ether iPrOMF, appeared at longer reaction times but in very minor amounts (Figure S11).

A further increase in Ni content (catalyst $\text{Ni}_{62}\text{Fe}_{38}/\text{SiO}_2$) led to a noticeably higher yield of FFA, making it the most selective catalyst in the series (0.45 mmol after 2 h of reaction with 10 mg of catalyst). However, FFA started to undergo secondary reactions when increasing the reaction time, mainly etherification to iPrOMF. In contrast, the amounts of THFFA and MF (maximum amounts, 0.025 and 0.035 mmol, respectively) were similar to those measured for $\text{Ni}_{55}\text{Fe}_{45}/\text{SiO}_2$.

MTHF remained a very minor product. The yields of FFA and, to a lesser extent, iPrOMF measured for $\text{Ni}_{73}\text{Fe}_{27}/\text{SiO}_2$ were quite similar to those measured for $\text{Ni}_{62}\text{Fe}_{38}/\text{SiO}_2$, making $\text{Ni}_{73}\text{Fe}_{27}/\text{SiO}_2$ the second most selective catalyst of the series with respect to FFA. However, the amounts of secondary and tertiary products, THFFA, MF, and MTHF, progressively increased as a function of (time \times mass), indicating that even a 10 atom % increase of Ni in the catalyst could favor side reactions.

A dramatic effect on the yield of FFA occurred for $\text{Ni}_{84}\text{Fe}_{16}/\text{SiO}_2$. FFA, which reached a yield of 0.335 mmol at its maximum, was now found to be rapidly consumed (above time \times mass = 5 h mg), mainly by etherification to iPrOMF, which ultimately became the major product of reaction. Hydrogenolysis to MF and, to a lesser extent, ring hydrogenation to THFFA also gradually affected the products slate, with final amounts of 0.089 and 0.081 mmol, respectively. Production of MTHF also increased, but this was not a major transformation pathway. The slight decrease in production of MF, whereas the production of THFFA increased almost linearly with time without presenting a maximum, suggests that MTHF was mainly produced by hydrogenation of the ring of MF.

The same tendencies were found for $\text{Ni}_{92}\text{Fe}_8/\text{SiO}_2$, with even earlier consumption of FFA and lower amounts of iPrOMF and MF. In this case, it was production of THFFA, the fully hydrogenated molecule, that increased dramatically; it became the predominant product along with iPrOMF. As a consequence, the ether associated with THFFA, iPrOMTHF, which could form by etherification of THFFA, now present in a large amount, or by ring hydrogenation of iPrOMF, was detected. In line with the higher activity in the ring hydrogenation pathway, the amount of MTHF increased slightly compared with $\text{Ni}_{84}\text{Fe}_{16}/\text{SiO}_2$. Here also, its production could be correlated with consumption of MF.

Finally, the trends for monometallic $\text{Ni}_{100}/\text{SiO}_2$ consisted of amplification of those identified for $\text{Ni}_{92}\text{Fe}_8/\text{SiO}_2$. FFA started to be consumed from (time \times mass) = 2.5 h mg. The three secondary products appeared as early as the first measurement, in the following decreasing amounts: iPrOMF, MF, and THFFA. MF and iPrOMF were progressively consumed, and only production of THFFA continued to increase until a plateau was reached. The associated ether, iPrOMTHF, appeared for (time \times mass) = 20 h mg via etherification of THFFA or ring hydrogenation of iPrOMF. Finally, the ring hydrogenation pathway led to a linear increase in MTHF production, which became the major product. The presence of a clear maximum for production of MF confirmed that MTHF was formed by hydrogenation of MF. However, the plateau reached for THFFA could also indicate that MTHF was partly formed via hydrogenolysis of THFFA. Overall, the $\text{Ni}_{100}/\text{SiO}_2$ catalyst was characterized by its high activity in the ring hydrogenation and hydrogenolysis pathways, with the former becoming predominant.

Selectivities obtained at full conversion for a mass of catalyst of 10 mg and a reaction time of 2 h are presented in [Table S11](#) to better show the influence of the increasing Ni proportion on catalytic performance.

Information about the recyclability of the $\text{Ni}_{62}\text{Fe}_{38}/\text{SiO}_2$ and $\text{Ni}_{100}/\text{SiO}_2$ catalysts is provided in [Table S12](#) and [Figures S12](#) and [S13](#). In particular, we confirmed that the LEIS spectrum recorded on twice-recycled $\text{Ni}_{62}\text{Fe}_{38}/\text{SiO}_2$ did not change significantly compared with that from the catalyst just after re-activation and prior to reaction ([Figures S12](#) and [S13](#)).

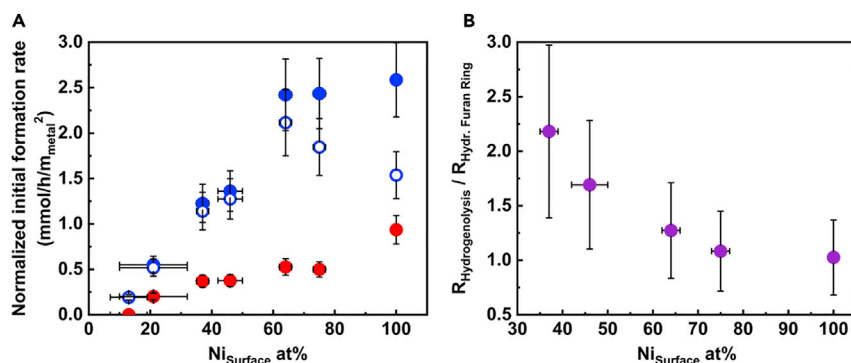


Figure 7. Initial rate of FF consumption, normalized with respect to the exposed metal surface area

(A) As a function of the nominal Ni molar proportion.

(B) As a function of the surface Ni molar proportion.

Error bars are drawn according to the standard deviation through 10 times computations at every point.

DISCUSSION

To get more insight into the nature of the active sites at the surface of the Ni-Fe nanoparticles, the initial rate of FF consumption (in other terms, the rate of hydrogenation of the aldehyde function) was calculated from the amount of FF remaining at (time × mass) = 1.5 h mg and was normalized with respect to the exposed metal surface area in square meters. An error bar was calculated based on a relative error of 5% on determination of the FF amount (repeatability of measurements), an absolute error of 4% on the metal content, and an absolute error of 1% on metal dispersion. The rate increased linearly with the Ni nominal molar proportion (Figure 7A). The intercept of this linear trend with the x axis is located above 0, suggesting that the rate is not strictly proportional to the number of Ni atoms and that a minimum amount of Ni is required to initiate hydrogenation of the aldehyde function.

This initial rate was then plotted as a function of the surface Ni molar proportion, using the quantification results by LEIS and the error bars presented above (Figure 7B). When focusing on the composition of the outer shells of the Ni-Fe nanoparticles, the trend is no longer linear, with a steeper slope in the lower Ni proportion range. Extrapolation of the trend may indicate that a minimum of 10 Ni atom % is required at the nanoparticle surface to catalyze hydrogenation. This pattern suggests that hydrogenation of the aldehyde function is linked to the existence of ensembles of Ni atoms in Fe-rich areas and that the effect of the growing connectivity between the neighboring Ni atoms is stronger at lower Ni content (high dilution of Ni with respect to Fe) and weaker at higher Ni content (for which large Ni domains already exist). These results do not point to the existence of specific, isolated Ni-Fe sites that would perform hydrogenation of the aldehyde function more rapidly on the bimetallic surfaces.

A comparison can be done with the influence of the surface Ni molar proportion on the formation rates of the different products. In Figure 8A, the products were grouped into two categories: those for which no secondary reaction with H₂ took place (FFA and iPrOMF, full blue circles) and those that underwent at least one step of hydrogenolysis or ring hydrogenation (MF, THFFA, and MTHF; full red circles).

The pattern concerning the initial neat formation rate of FFA (as such or under its ether form) is similar to the one found for consumption of FF. Values seem to reach

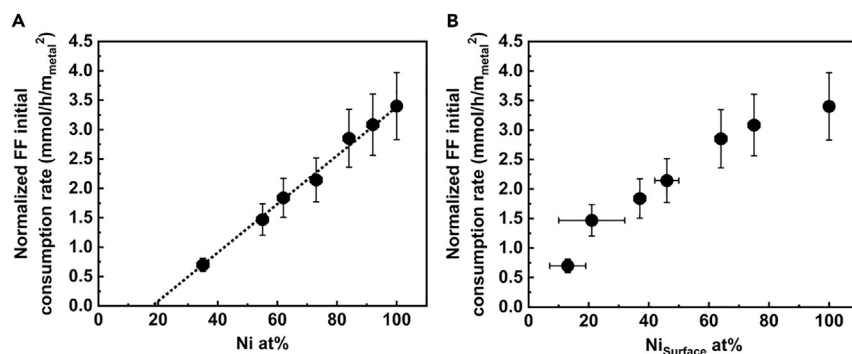


Figure 8. Rate of product formation

(A) Initial rate of product formation, normalized with respect to the exposed metal surface area, as a function of the surface Ni molar proportion.

(B) Ratio of the initial rate of hydrogenolysis and the initial rate of ring hydrogenation as a function of the surface Ni molar proportion.

Full blue circles, FFA + iPrOMF; open blue circles, FFA alone; red circles, MF + THFFA + MTHF. Error bars are drawn according to the standard deviation through 10 times computations at every point.

a plateau when the Ni proportion is high, as the consumption of FFA by hydrogenolysis or hydrogenation becomes prominent. Reaction rates of secondary processes involving H₂ also increase with the surface Ni molar proportion. A comparison of Figures 7B and 8A shows that, for Ni₅₅Fe₄₅/SiO₂, the ratio between the rate of hydrogenation of the aldehyde function and the total rate of the secondary hydroconversion processes is 7. This ratio falls to 4 on the monometallic Ni catalyst and ranges between 5 and 6 on the three intermediate systems. The extension of the Ni domains would thus favor the secondary processes of hydroconversion, in agreement with the fact that monometallic Ni is largely unselective. A more precise comparison is, however, difficult to make because, for Ni-rich catalysts, the initial production of iPrOMF is not negligible at short reaction times and how its production interferes with the hydroconversion route is not known (for instance, how the ether function can act as a protecting group with respect to secondary reactions).

Given the preferential formation of MTHF from MF with respect to THFFA, it could be assumed that the conversion of molecules containing a furan ring, such as MF, was favored on Ni-rich surfaces. Figure 8B reports the ratio between the initial rate of the hydrogenolysis route (formation of MF) and the initial rate of the ring hydrogenation route (formation of THFFA and MTHF) as a function of the surface Ni molar proportion. The ring hydrogenation route is not favored on Fe-rich surfaces, whereas the two routes co-exist to a similar extent on Ni-rich surfaces.

The most selective Ni-Fe catalysts to FFA, those containing a nominal Ni molar proportion of 60%–70% and exhibiting a surface molar proportion of 35%–45% Ni only, would thus be characterized by the existence of active sites consisting of limited Ni ensembles on which the hydrogenation of the aldehyde function of FF takes place at a moderate rate, hydrogenolysis of the oxygenated function takes place at a significantly slower rate, and hydrogenation of the furan ring would be the slowest route of all. Enriching the Ni-Fe surface in Ni results in an increase in the three reaction rates, with a large effect on the secondary hydroconversion pathways and especially the ring hydrogenation route. The size of Ni domains can influence activation of the reactants in two respects: the organic molecules, through adsorption limited to the polar function or involving the furan ring when the size of the ensemble increases, and

H₂, with a limitation of the amount of available H atoms. A comparison can be done with the distinction recently made in the literature between Ni edge and step sites, on which hydrogenation of FF would be limited to FFA, and flat Ni surfaces, on which hydrogenation of the furan ring would be favored.^{51,52} The existence of electronic effects in the bimetallic combinations cannot be excluded, but our observations do not provide conclusive elements regarding that point.

The gap in Figure 8A between the full blue circles (formation rate of FFA + iPrOMF) and the open blue circles (formation rate of FFA only) represents the initial formation rate of the ether, iPrOMF, which increases greatly when the Ni content increases in the catalyst. In contrast with the other pathways, etherification is expected to happen on unreduced metal ions acting as Lewis acidic centers rather than on metallic surfaces,^{53–55} and a correlation with the surface Ni content is probably not relevant. Identification of unreduced Ni²⁺ ions as possible active sites for etherification may sound counterintuitive because it was shown that Fe was the last metal to be reduced of the two during the initial reduction stage²³ and during re-activation in H₂ and that it was Ni that drove the reduction of Fe during re-activation (Figures 5 and S6). However, involvement of Ni²⁺ ions is hinted at by the non-negligible etherification of THFFA to iPrOMTHF on the monometallic Ni catalyst (Figure 6, Ni₁₀₀/SiO₂, blue dotted line). A minority of unreduced Ni²⁺ ions would not be detected by XAS, the only spectroscopy used here to follow the evolution of nickel, because the final XANES spectrum and EXAFS signal are dominated by the well-organized metallic phase. Despite a lack of direct evidence by characterization, the hypothesis of Ni²⁺ ions as active sites for etherification will be retained as a plausible one.

The reason why some Ni²⁺ ions would remain unreduced in the Ni-rich systems may be found in the poorer reducibility of Ni-rich phyllosilicates compared with Ni-Fe-containing phases, as can be inferred from temperature-programmed reduction profiles recorded on the solids after DPU synthesis (Figures S15 and S13). Although reduction of the metals is complete at 730°C for Ni₅₅Fe₄₅/SiO₂, Ni₆₂Fe₃₈/SiO₂, and Ni₇₃Fe₂₇/SiO₂, this is not the case for Ni₈₄Fe₁₆/SiO₂, Ni₉₂Fe₈/SiO₂ and especially Ni₁₀₀/SiO₂ (one should be aware that the conditions of reduction for TPR and for the catalyst preparation are different, with the latter involving a plateau at 700°C, and that direct extrapolation between the two reduction processes is not straightforward). Another hint can be found in the evolution of the specific surface area of the solids after reduction at 700°C (Table 1). It first increases to a maximum value for Ni₆₂Fe₃₈/SiO₂ and Ni₇₃Fe₂₇/SiO₂ and then decreases to reach a minimum for Ni₁₀₀/SiO₂. A similar pattern has been described for catalysts resulting from precipitation of Ni- and Fe-containing hydrotalcites.¹⁶ A high amount of Ni in the catalysts also favored side reactions of etherification with isopropanol, presumably through the presence of residual unreduced Ni²⁺ ions coming from difficult-to-reduce, well-organized phyllosilicate phases formed during synthesis by deposition-precipitation. The etherification pathway can be specific to catalysts prepared via an intermediate silicate phase and may not be seen when using Ni-Fe/SiO₂ catalysts prepared by impregnation.

Hydroconversion of FF in isopropanol was investigated using a series of Ni-Fe/SiO₂ and Ni/SiO₂ catalysts prepared by DPU and differing in the molar proportions of the two metals in the Ni-Fe nanoparticles, from Ni₃₅Fe₆₅ to Ni₁₀₀. All catalysts exhibited fcc alloyed nanoparticles with similar size distribution (4–7 nm), similar metal dispersion (17%–19%), and a homogeneous composition throughout a given catalyst (standard deviation: 7–8 Ni atom %). Reduced Ni-Fe nanoparticles were found to exhibit heterogeneities in their inner chemical order, and the nominal composition of the

catalyst did not reflect the composition of the outer shells of the nanoparticles. A gradient of Ni concentration was found from a Ni-enriched core to Ni-depleted, Fe-enriched outer shells, with a Ni depletion of 20%, on average, compared with the nominal composition, as determined from LEIS measurements. These outer shells readily oxidized upon exposure to dilute oxygen, but the Ni-Fe nanoparticles reverted to their former state upon re-activation in H₂ at 400°C, and no permanent dealloying was observed. The reduction of the metals started at a lower temperature when the Ni proportion increased. Fe-rich catalysts were poorly active in hydrogenation of FF but selective in FFA. Increasing the overall Ni proportion to 60–75 Ni atom % and the related surface composition of the nanoparticles to 35–45 Ni atom % provided the highest yield of FFA under the experimental conditions of the reaction. The active sites were supposed to consist of ensembles of Ni atoms whose limited size would decrease the availability of H₂ and inhibit planar adsorption of molecules possessing a furan ring compared with adsorption via the terminal polar functions. The rate of hydrogenation of the aldehyde function of FF and the rate of secondary processes involving H₂ (hydrogenolysis of the alcohol function, hydrogenation of the furan ring) increased when increasing the surface Ni proportion, with the latter progressively gaining prominence with formation of methylfuran, THFFA, and methyltetrahydrofuran, which became the major product with the monometallic Ni catalyst. A high amount of Ni in the catalysts also favored side reactions of etherification with isopropanol, possibly through the presence of residual Ni²⁺ ions coming from difficult-to-reduce, well-organized phyllosilicate phases formed during synthesis by deposition-precipitation.

The composition of the outer shells of Ni-Fe nanoparticles is thus linked to the global composition of the Ni-Fe nanoparticles and evolves following a similar trend but is not equal to it. More than specifically active surface sites or catalyst formulations, it is an adequate balance in the kinetics of the reactions enabled by the Ni ensembles located among Fe domains that allows hydrogenation of the aldehyde function of FF while limiting the reaction rate of secondary processes of hydrogenolysis and, especially, ring hydrogenation, linked to Ni-rich surfaces.

EXPERIMENTAL PROCEDURES

Resource availability

Lead contact

Further information and requests for resources should be directed to and will be fulfilled by the lead contact, E.M. (eric.marceau@univ-lille.fr).

Materials availability

All materials generated in this study are available from the [lead contact](#) with a completed materials transfer agreement.

Data and code availability

This study did not generate any datasets.

Catalyst preparation

Six Ni-Fe/SiO₂ catalysts differing by the proportions of the metals and a reference Ni/SiO₂ catalyst were prepared using a procedure of DPU on silica, described in detail elsewhere.²³ Nickel (II) and iron (II) sulfates (Aldrich, 99%, and Alfa Aesar, 98%, respectively) were used as precursor salts and Sipernat-50 silica as support (Degussa; surface area, 400 m² g⁻¹; pore volume, 1.4 cm³ g⁻¹). The total Ni + Fe concentration in the DPU solution was constant for the seven syntheses (0.28 mol L⁻¹). The molar proportions of Ni and Fe in solution are presented in [Table 1](#) for each preparation.

The initial DPU suspension containing silica, sulfuric acid (Alfa Aesar, 93%–98%), urea (Alfa Aesar, 99%–100%) and nickel sulfate was degassed with Ar before introduction of iron sulfate and heated to 80°C. An atmosphere of Ar was maintained during the 22 h of deposition-precipitation to avoid oxidation of Fe^{2+} to Fe^{3+} and separate precipitation of iron (III) compounds. After filtration and drying at room temperature under Ar, storage took place in air, which resulted in quantitative oxidation of Fe^{2+} to Fe^{3+} , as verified by Mössbauer spectroscopy (Figure S16). In all cases, powder XRD (diffraction peaks at $2\theta = 8.17^\circ$, 16.39° , and 24.69°) and ^{57}Fe Mössbauer spectroscopy applied to the dried solids confirmed formation of poorly organized 1:1 phyllosilicates containing Fe^{3+} . The association between Fe^{3+} and Ni^{2+} ions in the mixed phyllosilicates was evidenced via the linear decrease of the average quadrupole shift of Fe^{3+} when the Ni fraction increased, which would not occur if Fe^{3+} was present in the segregated ferric phases only (Table S14). Preparation of the catalysts ended with a reduction step of the dried solids in a flow of 10% H_2/Ar (100 mL min^{-1}) at 5°C min^{-1} up to 700°C with a plateau of 2 h without preliminary calcination. This temperature was chosen to ensure reduction of Fe to the metallic state.²³

Characterization of the catalysts

Elemental analysis was performed by XRF for determination of the metal content in reduced catalysts. Molar proportions were corroborated by ICP-OES measurements on the dried solids. On the basis of the dispersion of measurements for individual XRF scans, absolute errors were conservatively estimated to be $\pm 4\%$. The total metal loadings and molar proportions of Ni and Fe (calculated as $\text{Ni}/[\text{Ni} + \text{Fe}]$ and $\text{Fe}/[\text{Ni} + \text{Fe}]$) are presented in Table 1. Catalysts will be denoted using these measured molar proportions: $\text{Ni}_x\text{Fe}_{(100-x)}/\text{SiO}_2$. Except for $\text{Ni}_{35}\text{Fe}_{65}/\text{SiO}_2$, whose total metal content is significantly larger than that of the next ones in the series, metal loadings were found to increase in the 49–59 wt % range when the Ni molar proportion increased. As observed previously,²³ nickel was deposited preferentially with respect to iron during the DPU process; the nickel molar proportion on the catalyst was almost always larger than that of the corresponding DPU solution. The Ni proportion in the solids increased monotonically when the Ni fraction in the DPU solution increased, and the result was a series of Ni-Fe catalysts that displayed an increasing proportion of nickel and, conversely, a decreasing proportion of iron.

^{57}Fe Mössbauer spectra were measured with a source of ^{57}Co embedded in a rhodium metal matrix. Measurements were performed in transmission mode with the source at room temperature (Figure S16). The measured sample, in the form of powder, was mounted in a gas flow reactor working at controlled temperatures up to 700°C under diluted H_2 (5%)/Ar flow (flow rate, 50 mL min^{-1}). The sample was then transferred into an appropriate airtight sample holder within an Ar-filled glove box (O_2 , $\text{H}_2\text{O} < 1\text{ ppm}$) to avoid exposure to ambient air and to a helium gas flow cryostat for measurement at -268°C (5 K). For two catalysts, the airtight holder was then opened for exposure to ambient air. The sample was recovered, remounted in the gas flow reactor, and re-activated at 400°C under diluted H_2 flow before measuring a Mössbauer spectrum at 5 K as described above, strictly avoiding any contact with ambient air. The spectrometer was operated with a triangular velocity waveform, and a gas-filled proportional counter was used for detection of gamma rays. Velocity calibration was performed with an $\alpha\text{-Fe}$ foil. The isomer shift δ , the electric quadrupole splitting Δ , the magnetic hyperfine field B_{HF} , the line width at half maximum Γ , and the relative absorption area of the different components were determined by fitting the spectra to appropriate combinations of Lorentzian profiles. The isomer shifts are given relative to $\alpha\text{-Fe}$ at room temperature.

Time-resolved XAS data were obtained in transmission mode at the ROCK beamline (synchrotron SOLEIL) using a home-made Quick-EXAFS monochromator equipped with a Si (111) channel-cut crystal.^{56,57} The channel-cut oscillates with a $\pm 1.95^\circ$ amplitude around 14.6° and with a frequency of 2 Hz, allowing simultaneous recording of the Fe (7,112 eV) and Ni (8,333 eV) K-edge spectra in 250 ms. Successive spectra collected with upward Bragg angles during *in situ* monitoring of catalysts were merged to improve the signal-to-noise ratio, leading to a time resolution of 5 s per spectrum effectively analyzed. Ionization chambers provided by Ohyo Koken Kogyo, filled with a 2:1 mixture of N₂ and He, were used for measurements. The beam size was 2.5 × 0.5 mm. *In situ* re-activation of reduced catalysts previously exposed to ambient air was performed by heating the Lytle-type cell containing the sample from room temperature to 500°C under a H₂ (5%)/He flow (50 mL min⁻¹) with a heating rate of 5 °C min⁻¹. Oxidation of two reduced catalysts was performed at 80°C under an O₂ (10%)/He flow (35 mL min⁻¹) after a purge under N₂ (30 mL min⁻¹). Normalization of spectra was performed using the Python normal_gui graphical interface developed at SOLEIL for fast handling of Quick-XAS data.⁵⁸ The proportions of the different Fe and Ni species were determined by multivariate data analysis, the MCR-ALS method.^{59–61} MCR-ALS GUI 2.0, developed by Jaumot et al.⁶² and freely available as a MATLAB toolbox, was used for MCR-ALS analysis. EXAFS signal extraction and Fourier transform of the EXAFS spectra were done using the Athena graphical interface software.⁶³ EXAFS fitting of interatomic distances, coordination numbers, and Debye-Waller factors was performed with the Artemis interface to IFEFFIT (interactive EXAFS analysis and fitting) using least-squares refinements,⁶⁴ first checked on NiO, Ni metallic foil, and Fe₂O₃ references. Fourier-transformed EXAFS signals are presented without phase correction.

The LEIS analyses were performed on a Qtac100 spectrometer (IONTOF) following a protocol described previously.⁶⁵ A 5-keV Ne⁺ beam at normal incidence was selected for quantitative Fe and Ni analyses (1-nA beam current).⁶⁶ Prior to LEIS measurements, samples previously reduced at 700°C and exposed to air were re-activated *in situ* under pure hydrogen at 400°C for 2 h in a dedicated cell coupled to the spectrometer, allowing transfer under an ultra-high vacuum without air contamination. The ionic dose per spectrum was first limited to 0.05×10^{15} ions cm⁻² for the first 10 spectra (theoretically, each corresponding to 5% of a monolayer of a flat surface assumed to exhibit 10^{15} atoms cm⁻²) and then was increased to 1.2×10^{15} ions cm⁻² to complete analysis of the surface and analyze the composition of the subsurface. The data were processed using the SurfaceLab software from the same manufacturer. The LEIS signal was decomposed using the experimental line shapes provided by the Fe and Ni peaks of the Fe₂O₃ and NiO reference materials (at 1,202 and 1,289 eV, respectively) to take into account the isotopic distribution of each metal. During the measurements, the Fe peak was found at $1,210 \pm 10$ eV and the Ni peak at $1,290 \pm 10$ eV; these intervals result from differences in charge compensation. The ratio of the sensitivity factors $\eta(\text{Fe})/\eta(\text{Ni})$, used for the relative quantification of the two metals, was previously determined to be equal to 0.89.⁶⁵

SUPPLEMENTAL INFORMATION

Supplemental information can be found online at <https://doi.org/10.1016/j.checat.2022.04.009>.

ACKNOWLEDGMENTS

This work has benefitted from support of the CSC-Centrale Lille PhD scholarship program (to D.S.) and the French National Research Agency (ANR) through the

NobleFreeCat project (ANR-17-CE07-0022). We thank the Chevreul Institute and the TEM facility in Lille for help with development of this work through the ARCHICM project supported by the “Ministère de l’Enseignement supérieur, de la Recherche et de l’Innovation”, the region “Hauts-de-France”, the ERDF program of the European Union, and the “Métropole Européenne de Lille”. XAS experiments were performed on the ROCK beamline, using the Chemistry support lab, at SOLEIL Synchrotron, France (beamtime allocated for proposal numbers 20151218 and 20161106). The ROCK (Rocking Optics for Chemical Kinetic) beamline at SOLEIL (Source Optimisée de Lumière d’Énergie Intermédiaire du LURE) Synchrotron is benefitting from a public grant overseen by the French National Research Agency as a part of the “Investissements d’Avenir” program (PIA) with the contractual reference “ANR-10-EQPX-45.” The REALCAT platform is benefitting from a state subsidy administrated by the French National Research Agency within the frame of the “Future Investments” program (PIA) with the contractual reference “ANR-11-EQPX-0037.” The European Union, through ERDF funding administered by the Hauts-de-France region, has co-financed the platform. We thank Centrale Lille, the CNRS, and University of Lille as well as the Centrale Initiatives Foundation for financial contributions to acquisition and implementation of equipment. We thank the “Réseau des Rayons X et Gamma” (Université Montpellier, France) for granting access to their Mössbauer spectroscopy platform. We also thank Joëlle Thuriot-Roukos (XRF, ICP-OES), Olivier Gardoll (TPR), Svetlana Heyte (SPR/GC-MS), and Jérémy Dhainaut (bright-field TEM measurements), all at UCCS, for their help.

AUTHOR CONTRIBUTIONS

The manuscript was written through contributions of all authors. D.S. was a PhD candidate who prepared the catalysts; characterized them by XRD, TEM, N₂ physisorption, and TPR; performed the catalytic tests; and wrote the first draft of the manuscript. A.S. was a postdoctoral fellow who performed the recycling experiments. J.-S.G., C.C., and E.M. participated in the *in situ* XAS measurements, headed by C.L.F. at synchrotron SOLEIL. A.-S.M. performed the LEIS measurements and analyzed the data. M.M. performed the STEM-HR-EELS measurements and analyzed the data. L.S. analyzed the Mössbauer spectra and wrote the corresponding sections. M.T.S. recorded the Mössbauer spectra. R.W., S.P., and E.M. supervised D.S. and A.S., and all three contributed to revision of the catalysis sections. R.W. supervised the catalytic tests and analysis by XRF, revised the manuscript, and performed the complete revision of the manuscript in its final form. E.M. analyzed the XAS data, wrote the corresponding sections, revised the characterization sections, and performed the complete revision of the manuscript in its final form. All authors have given approval to the final version of the manuscript.

DECLARATION OF INTERESTS

The authors declare no competing interests.

Received: February 12, 2022

Revised: March 23, 2022

Accepted: April 15, 2022

Published: May 9, 2022

REFERENCES

1. Brownlee, H.J., and Miner, C.S. (1948). Industrial development of furfural. *Ind. Eng. Chem.* 40, 201–204. <https://doi.org/10.1021/ie50458a005>.
2. Yan, K., Wu, G., Lafleur, T., and Jarvis, C. (2014). Production, properties and catalytic hydrogenation of furfural to fuel additives and value-added chemicals. *Renew. Sustain. Energy Rev.* 38, 663–676. <https://doi.org/10.1016/j.rser.2014.07.003>.

3. Li, X., Jia, P., and Wang, T. (2016). Furfural: a promising platform compound for sustainable production of C4 and C5 chemicals. *ACS Catal.* 6, 7621–7640. <https://doi.org/10.1021/acscatal.6b01838>.
4. Chen, S., Wojcieszak, R., Dumeignil, F., Marceau, E., and Royer, S. (2018). How catalysts and experimental conditions determine the selective hydroconversion of furfural and 5-hydroxymethylfurfural. *Chem. Rev.* 118, 11023–11117. <https://doi.org/10.1021/acs.chemrev.8b00134>.
5. Halilu, A., Ali, T.H., Atta, A.Y., Sudarsanam, P., Bhargava, S.K., and Abd Hamid, S.B. (2016). Highly selective hydrogenation of biomass-derived furfural into furfuryl alcohol using a novel magnetic nanoparticles catalyst. *Energy Fuel.* 30, 2216–2226. <https://doi.org/10.1021/acs.energyfuels.5b02826>.
6. Liu, L., Liu, H., Huang, W., He, Y., Zhang, W., Wang, C., and Lin, H. (2017). Mechanism and kinetics of the electrocatalytic hydrogenation of furfural to furfuryl alcohol. *J. Electroanal. Chem.* 804, 248–253. <https://doi.org/10.1016/j.jelechem.2017.09.021>.
7. Li, H., Luo, H., Zhuang, L., Dai, W., and Qiao, M. (2003). Liquid phase hydrogenation of furfural to furfuryl alcohol over the Fe-promoted Ni-B amorphous alloy catalysts. *J. Mol. Catal. A. Chem.* 203, 267–275. [https://doi.org/10.1016/S1381-1169\(03\)00368-6](https://doi.org/10.1016/S1381-1169(03)00368-6).
8. Nguyen-Huy, C., Kim, J.S., Yoon, S., Yang, E., Kwak, J.H., Lee, M.S., and An, K. (2018). Supported Pd nanoparticle catalysts with high activities and selectivities in liquid-phase furfural hydrogenation. *Fuel* 226, 607–617. <https://doi.org/10.1016/j.fuel.2018.04.029>.
9. Goh, T.W., Tsung, C.K., and Huang, W. (2019). Spectroscopy identification of the bimetallic surface of metal-organic framework-confined Pt-Sn nanoclusters with enhanced chemoselectivity in furfural hydrogenation. *ACS Appl. Mater. Inter.* 11, 23254–23260. <https://doi.org/10.1021/acsaami.9b06229>.
10. Lee, J., Woo, J., Nguyen-Huy, C., Lee, M.S., Joo, S.H., and An, K. (2020). Highly dispersed Pd catalysts supported on various carbons for furfural hydrogenation. *Catal. Today* 350, 71–79. <https://doi.org/10.1016/j.cattod.2019.06.032>.
11. Yan, H., Lv, H., Yi, H., Liu, W., Xia, Y., Huang, X., Huang, W., Wei, S., Wu, X., and Lu, J. (2018). Understanding the underlying mechanism of improved selectivity in Pd₂ single-atom catalyzed hydrogenation reaction. *J. Catal.* 366, 70–79. <https://doi.org/10.1016/j.jcat.2018.07.033>.
12. Pirmoradi, M., and Kastner, J.R.A. (2021). Kinetic model of multi-step furfural hydrogenation over a Pd-TiO₂ supported activated carbon catalyst. *Chem. Eng. J.* 414, 128693. <https://doi.org/10.1016/j.cej.2021.128693>.
13. Li, S., Dong, M., Yang, J., Cheng, X., Shen, X., Liu, S., Wang, Z.Q., Gong, X.Q., Liu, H., and Han, B. (2021). Selective hydrogenation of 5-(Hydroxymethyl)Furfural to 5-methylfurfural over single atomic metals anchored on Nb₂O₅. *Nat. Comm.* 12, 584. <https://doi.org/10.1038/s41467-020-20878-7>.
14. Jiménez-Gómez, C.P., Defilippi, C., Cecilia, J.A., Moreno-Tost, R., Maireles-Torres, P., and Giordano, C. (2020). The role of nitride species in the gas-phase furfural hydrogenation activity of supported nickel catalysts. *Mol. Catal.* 487, 110889. <https://doi.org/10.1016/j.mcat.2020.110889>.
15. Xu, J., Cui, Q., Xue, T., Guan, Y., and Wu, P. (2020). Total hydrogenation of furfural under mild conditions over a durable Ni/TiO₂-SiO₂ catalyst with amorphous TiO₂ species. *ACS Omega* 5, 30257–30266. <https://doi.org/10.1021/acsomega.0c04736>.
16. Shao, Y., Wang, J., Sun, K., Gao, G., Li, C., Zhang, L., Zhang, S., Xu, L., Hu, G., and Hu, X. (2021). Selective hydrogenation of furfural and its derivative over bimetallic NiFe-based catalysts: understanding the synergy between Ni sites and Ni-Fe alloy. *Renew. Energy* 170, 1114–1128. <https://doi.org/10.1016/j.renene.2021.02.056>.
17. Pomeroy, B., Grilc, M., Gyergyek, S., and Likozar, B. (2021). Catalyst structure-based hydroxymethylfurfural (HMF) hydrogenation mechanisms, activity and selectivity over Ni. *Chem. Eng. J.* 412, 127553. <https://doi.org/10.1016/j.cej.2020.127553>.
18. Sunyol, C., English Owen, R., González, M.D., Salagre, P., and Cesteros, Y. (2021). Catalytic hydrogenation of furfural to tetrahydrofurfuryl alcohol using competitive nickel catalysts supported on mesoporous clays. *Appl. Catal. A. Gen.* 611, 117903. <https://doi.org/10.1016/j.apcata.2020.117903>.
19. Chen, S.H., Tseng, Y.C., Yang, S.C., and Lin, S.D. (2021). Investigating hydrogenation and decarbonylation in vapor-phase furfural hydrotreating over Ni/SiO₂ catalysts: propylene production. *Appl. Catal. A. Gen.* 613, 118020. <https://doi.org/10.1016/j.apcata.2021.118020>.
20. Yu, X., Chen, J., and Ren, T. (2014). Promotional effect of Fe on performance of Ni/SiO₂ for deoxygenation of methyl laurate as a model compound to hydrocarbons. *RSC Adv.* 4, 46427–46436. <https://doi.org/10.1039/c4ra07932a>.
21. Putro, W.S., Kojima, T., Hara, T., Ichikuni, N., and Shimazu, S. (2017). Selective hydrogenation of unsaturated carbonyls by Ni-Fe-based alloy catalysts. *Catal. Sci. Technol.* 7, 3637–3646. <https://doi.org/10.1039/c7cy00945c>.
22. Jiménez-Gómez, C.P., Cecilia, J.A., García-Sancho, C., Moreno-Tost, R., and Maireles-Torres, P. (2019). Selective production of furan from gas-phase furfural decarbonylation on Ni-MgO catalysts. *ACS Sustain. Chem. Eng.* 7, 7676–7685. <https://doi.org/10.1021/acssuschemeng.8b06155>.
23. Shi, D., Yang, Q., Peterson, C., Lamic-Humblot, A.F., Girardon, J.S., Griboval-Constant, A., Stievano, L., Sougrati, M.T., Briois, V., Bagot, P.A.J., et al. (2019). Bimetallic Fe-Ni/SiO₂ catalysts for furfural hydrogenation: identification of the interplay between Fe and Ni during deposition-precipitation and thermal treatments. *Catal. Today* 334, 162–172. <https://doi.org/10.1016/j.cattod.2018.11.041>.
24. Chieffi, G., Giordano, C., Antonietti, M., and Esposito, D. (2014). FeNi nanoparticles with carbon armor as sustainable hydrogenation catalysts: towards biorefineries. *J. Mater. Chem. A* 2, 11591–11596. <https://doi.org/10.1039/c4ta02457e>.
25. Jia, P., Lan, X., Li, X., and Wang, T. (2018). Highly active and selective NiFe/SiO₂ bimetallic catalyst with Optimized solvent effect for the liquid-phase hydrogenation of furfural to furfuryl alcohol. *ACS Sustain. Chem. Eng.* 6, 13287–13295. <https://doi.org/10.1021/acssuschemeng.8b02876>.
26. Jia, P., Lan, X., Li, X., and Wang, T. (2019). Highly selective hydrogenation of furfural to cyclopentanone over a NiFe bimetallic catalyst in a methanol/water solution with a solvent effect. *ACS Sustain. Chem. Eng.* 7, 15221–15229. <https://doi.org/10.1021/acssuschemeng.9b02112>.
27. Sitthisa, S., An, W., and Resasco, D.E. (2011). Selective conversion of furfural to methylfuran over silica-supported NiFe bimetallic catalysts. *J. Catal.* 284, 90–101. <https://doi.org/10.1016/j.jcat.2011.09.005>.
28. Wang, C., Luo, J., Liao, V., Lee, J.D., Onn, T.M., Murray, C.B., and Gorte, R.J. (2018). A comparison of furfural hydrodeoxygenation over Pt-Co and Ni-Fe catalysts at high and low H₂ pressures. *Catal. Today* 302, 73–79. <https://doi.org/10.1016/j.cattod.2017.06.042>.
29. Shi, D., Wojcieszak, R., Paul, S., and Marceau, E. (2019). Ni promotion by Fe: what benefits for catalytic hydrogenation? *Catalysts* 9, 451–477. <https://doi.org/10.3390/catal9050451>.
30. Yu, W., Xiong, K., Ji, N., Porosoff, M.D., and Chen, J.G. (2014). Theoretical and experimental studies of the adsorption geometry and reaction pathways of furfural over FeNi bimetallic model surfaces and supported catalysts. *J. Catal.* 317, 253–262. <https://doi.org/10.1016/j.jcat.2014.06.025>.
31. Liu, X., An, W., Turner, C.H., and Resasco, D.E. (2018). Hydrodeoxygenation of M-cresol over bimetallic NiFe alloys: kinetics and thermodynamics insight into reaction mechanism. *J. Catal.* 359, 272–286. <https://doi.org/10.1016/j.jcat.2018.01.006>.
32. Nie, L., de Souza, P.M., Noronha, F.B., An, W., Sooknoi, T., and Resasco, D.E. (2014). Selective conversion of M-cresol to toluene over bimetallic Ni-Fe catalysts. *J. Mol. Catal. A. Chem.* 388–389, 47–55. <https://doi.org/10.1016/j.molcata.2013.09.029>.
33. Jiang, Z., Wan, W., Lin, Z., Xie, J., and Chen, J.G. (2017). Understanding the role of M/Pt(111) (M = Fe, Co, Ni, Cu) bimetallic surfaces for selective hydrodeoxygenation of furfural. *ACS Catal.* 7, 5758–5765. <https://doi.org/10.1021/acscatal.7b01682>.
34. Kumbhar, P.S., Kharkar, M.R., Yadav, G.D., and Rajadhyaksha, R.A. (1992). Geometric and electronic effects in silica supported bimetallic nickel-copper and nickel-iron catalysts for liquid-phase hydrogenation of acetophenone and benzonitrile. *J. Chem. Soc. Chem. Comm.* 7, 584–586. <https://doi.org/10.1039/C39920000584>.
35. Unmuth, E.E., Schwartz, L.H., and Butt, J.B. (1980). Iron alloy Fischer-Tropsch catalysts I. Oxidation-reduction studies of the

- Fe₂Sb₂Ni system. *J. Catal.* **61**, 242–255. [https://doi.org/10.1016/0021-9517\(80\)90360-7](https://doi.org/10.1016/0021-9517(80)90360-7).
36. Tomishige, K., Li, D., Tamura, M., and Nakagawa, Y. (2017). Nickel-iron alloy catalysts for reforming of hydrocarbons: preparation, structure, and catalytic properties. *Catal. Sci. Technol.* **7**, 3952–3979. <https://doi.org/10.1039/c7cy01300k>.
37. Mutz, B., Belimov, M., Wang, W., Sprenger, P., Serrer, M.A., Wang, D., Pfeifer, P., Kleist, W., and Grunwaldt, J.D. (2017). Potential of an alumina-supported Ni₃Fe catalyst in the methanation of CO₂: impact of alloy formation on activity and stability. *ACS Catal.* **7**, 6802–6814. <https://doi.org/10.1021/acscatal.7b01896>.
38. Han, Q., Rehman, M.U., Ur Rehman, M., Wang, J., Rykov, A., Gutiérrez, O.Y., Zhao, Y., Wang, Sh., Ma, X., and Lercher, J.A. (2019). The synergistic effect between Ni sites and Ni-Fe alloy sites on hydrodeoxygenation of lignin-derived phenols. *Appl. Catal. B. Env.* **253**, 348–358. <https://doi.org/10.1016/j.apcatb.2019.04.065>.
39. Margossian, T., Larmier, K., Kim, S.M., Krumeich, F., Müller, C., and Copéret, C. (2017). Supported bimetallic NiFe nanoparticles through colloid synthesis for improved dry reforming performance. *ACS Catal.* **7**, 6942–6948. <https://doi.org/10.1021/acscatal.7b02091>.
40. Ashok, J., and Kawi, S. (2014). Nickel-iron alloy supported over iron-alumina catalysts for steam reforming of biomass tar model compound. *ACS Catal.* **4**, 289–301. <https://doi.org/10.1021/cs400621p>.
41. Gil, A., Díaz, A., Gandía, L.M., and Montes, M. (1994). Influence of the preparation method and the nature of the support on the stability of nickel catalysts. *Appl. Catal. A. Gen.* **109**, 167–179. [https://doi.org/10.1016/0926-860X\(94\)80116-9](https://doi.org/10.1016/0926-860X(94)80116-9).
42. Marceau, E., Löfberg, A., Giraudon, J.M., Négrier, F., Che, M., and Leclercq, L. (2009). From Al₂O₃-supported Ni(II)-Ethylenediamine complexes to CO hydrogenation catalysts: characterization of the surface sites and catalytic properties. *Appl. Catal. A. Gen.* **362**, 34–39. <https://doi.org/10.1016/j.apcata.2009.04.029>.
43. Johnson, C.E., Ridout, M.S., and Cranshaw, T.E. (1963). The Mossbauer effect in iron alloys. *Proc. Phys. Soc.* **81**, 1079–1090. <https://doi.org/10.1088/0370-1328/81/6/313>.
44. Nagorny, K., and Bubert, S. (1987). Möbauer spectroscopic investigations of bimetallic FeCo, FeNi, and FeRu model catalysts supported on magnesium hydroxide carbonate. *J. Catal.* **108**, 112–134. [https://doi.org/10.1016/0021-9517\(87\)90159-X](https://doi.org/10.1016/0021-9517(87)90159-X).
45. Li, T., Wang, H., Yang, Y., Xiang, H., and Li, Y. (2014). Study on an iron-nickel bimetallic Fischer-Tropsch synthesis catalyst. *Fuel Process. Technol.* **118**, 117–124. <https://doi.org/10.1016/j.fuproc.2013.08.015>.
46. Brown, R., Cooper, M.E., and Whan, D.A. (1982). Temperature programmed reduction of alumina supported iron, cobalt and nickel bimetallic catalysts. *Appl. Catal.* **3**, 177–186. [https://doi.org/10.1016/0166-9834\(82\)80090-0](https://doi.org/10.1016/0166-9834(82)80090-0).
47. Serrer, M.-A., Gaur, A., Jelic, J., Weber, S., Fritsch, Ch., Clark, A.H., Clark, A., Saraçi, E., Studt, F., and Grunwaldt, J.-D. (2020). Structural dynamics in Ni-Fe catalysts during CO₂ methanation – role of iron oxide clusters. *Catal. Sci. Technol.* **10**, 7542–7554. <https://doi.org/10.1039/D0CY01396J>.
48. Rao, Z., Cao, Y., Huang, Z., Yin, Z., Wan, W., Ma, M., Wu, Y., Wang, J., Yang, G., Cui, Y., et al. (2021). Insights into the nonthermal effects of light in dry reforming of methane to enhance the H₂/CO ratio near unity over Ni/Ga₂O₃. *ACS Catal.* **11**, 4730–4738. <https://doi.org/10.1021/acscatal.0c04826>.
49. Mizushima, T., Tohji, K., Udagawa, Y., Harada, M., Ishikawa, M., and Ueno, A. (1988). Characterization of silica-supported bimetallic iron-nickel catalysts by EXAFS. *J. Catal.* **112**, 282–289. [https://doi.org/10.1016/0021-9517\(88\)90140-6](https://doi.org/10.1016/0021-9517(88)90140-6).
50. Fang, H., Zheng, J., Luo, X., Du, J., Roldan, A., Leoni, S., and Yuan, Y. (2017). Product tunable behavior of carbon nanotubes-supported Ni-Fe catalysts for guaiacol hydrodeoxygenation. *Appl. Catal. A. Gen.* **529**, 20–31. <https://doi.org/10.1016/j.apcata.2016.10.011>.
51. Meng, X., Yang, Y., Chen, L., Xu, M., Zhang, X., and Wei, M. (2019). A control over hydrogenation selectivity of furfural via tuning exposed facet of Ni catalysts. *ACS Catal.* **9**, 4226–4235. <https://doi.org/10.1021/acscatal.9b00238>.
52. Chen, L., Ye, J., Yang, Y., Yin, P., Feng, H., Chen, C., Zhang, X., Wei, M., and Truhlar, D.G. (2020). Catalytic conversion furfuryl alcohol to tetrahydrofurfuryl alcohol and 2-methylfuran at terrace, step, and corner sites on Ni. *ACS Catal.* **10**, 7240–7249. <https://doi.org/10.1021/acscatal.0c01441>.
53. Li, X.L., Zhang, K., Chen, S.Y., Li, C., Li, F., Xu, H.J., and Fu, Y. (2018). A cobalt catalyst for reductive etherification of 5-hydroxymethylfurfural to 2,5-bis(Methoxymethyl)Furan under mild conditions. *Green. Chem.* **20**, 1095–1105. <https://doi.org/10.1039/C7GC03072J>.
54. Koehle, M., and Lobo, R.F. (2016). Lewis acidic Zeolite beta catalyst for the meerwein-ponndorf-Verley reduction of furfural. *Catal. Sci. Technol.* **6**, 3018–3026. <https://doi.org/10.1039/c5cy01501d>.
55. Natsir, T.A., and Shimazu, S. (2020). Fuels and fuel additives from furfural derivatives via etherification and formation of methylfurans. *Fuel Process. Technol.* **200**, 106308. <https://doi.org/10.1016/j.fuproc.2019.106308>.
56. Briois, V., La Fontaine, C., Belin, S., Barthe, L., Moreno, T., Pinty, V., Carcy, A., Girardot, R., and Fonda, E. (2016). ROCK: the new quick-EXAFS beamline at SOLEIL. *J. Phys. Conf. Ser.* **712**, 012149. <https://doi.org/10.1088/1742-6596/712/1/012149>.
57. Fonda, E., Rochet, A., Ribbens, M., Barthe, L., Belin, S., and Briois, V. (2012). The SAMBA quick-EXAFS monochromator: XAS with edge jumping. *J. Synchrotron Radiat.* **19**, 417–424. <https://doi.org/10.1107/S0909049512009703>.
58. Lesage, C., Devers, E., Legens, C., Fernandes, G., Roudenko, O., and Briois, V. (2019). High pressure cell for edge jumping X-ray absorption spectroscopy: applications to industrial liquid sulfidation of hydrotreatment catalysts. *Catal. Today* **336**, 63–73. <https://doi.org/10.1016/j.cattod.2019.01.081>.
59. Cassinelli, W.H., Martins, L., Passos, A.R., Pulcinelli, S.H., Santilli, C.V., Rochet, A., and Briois, V. (2014). Multivariate curve resolution analysis applied to time-resolved synchrotron X-ray absorption spectroscopy monitoring of the activation of copper alumina catalyst. *Catal. Today* **229**, 114–122. <https://doi.org/10.1016/j.cattod.2013.10.077>.
60. Hong, J., Marceau, E., Khodakov, A.Y., Gaberová, L., Griboval-Constant, A., Girardon, J.S., La Fontaine, C., and Briois, V. (2015). Speciation of ruthenium as a reduction promoter of silica-supported Co catalysts: a time-resolved in situ XAS investigation. *ACS Catal.* **5**, 1273–1282. <https://doi.org/10.1021/cs501799p>.
61. Rochet, A., Baubet, B., Moizan, V., Pichon, C., and Briois, V. (2016). Co-K and Mo-K edges quick-XAS study of the sulfidation properties of Mo/Al₂O₃ and CoMo/Al₂O₃ catalysts. *Compt. Rendus Chim.* **19**, 1337–1351. <https://doi.org/10.1016/j.crci.2016.01.009>.
62. Jaumot, J., de Juan, A., and Tauler, R. (2015). MCR-ALS GUI 2.0: new features and applications. *Chemom. Intell. Lab. Syst.* **140**, 1–12. <https://doi.org/10.1016/j.chemolab.2014.10.003>.
63. Ravel, B., and Newville, M. (2005). ATHENA, ARTEMIS, HEPHAESTUS: data analysis for X-ray absorption spectroscopy using IFEFFIT. *J. Synchrotron Radiat.* **12**, 537–541. <https://doi.org/10.1107/S0909049505012719>.
64. Newville, M. (2001). IFEFFIT: interactive XAFS analysis and FEFF fitting. *J. Synchrotron Rad.* **8**, 322–324. <https://doi.org/10.1107/S0909049500016964>.
65. Sadier, A., Shi, D., Mamede, A.S., Paul, S., Marceau, E., and Wojcieszak, R. (2021). Selective aqueous phase hydrogenation of xylose to xylitol over SiO₂-supported Ni and Ni-Fe catalysts: benefits of promotion by Fe. *Appl. Catal. B Environ.* **298**, 120564. <https://doi.org/10.1016/j.apcatb.2021.120564>.
66. Chernysh, V.S., Brongersma, H.H., Brüner, P., and Grehl, T. (2019). Surface composition of ion bombarded nickel based alloys. *Nucl. Instrum. Methods Phys. Res. Sect. B Beam Interact. Mater. Atoms* **460**, 180–184. <https://doi.org/10.1016/j.nimb.2019.02.008>.